UNIVERSITÀ DEGLI STUDI DI PAVIA

DIPARTIMENTO DI FISICA

Laurea Magistrale in Scienze Fisiche

Computational Dosimetry for in-vivo BNCT using accelerator based epithermal beams

MSc thesis by:
Emilia Dottorini

Supervisor:
Prof. Silva Bortolussi
Co-supervisors:
Dr. Hanna Koivunoro
Dr. Cristina Pezzi

A.Y. 2024-2025

Abstract

Il presente studio approfondisce la dosimetria computazionale applicata alla Boron Neutron Capture Therapy (BNCT) per esperimenti radiobiologici in vivo, utilizzando sorgenti di neutroni epitermici prodotte da acceleratore. Tali sorgenti sono i fasci già operanti o in costruzione per la BNCT clinica dei pazienti. Le sorgenti menzionate nella tesi sono il fascio clinico dell'ospedale di Helsinki, generato dall'acceleartore di Neutron Therapeutics, e il fascio clinico progettato e in fase di costruzione in Italia (progetto PNC-PNRR Anthem). In una prima fase, è stato condotto uno studio preliminare di un *holder* per l'irraggiamento degli animali, con il duplice scopo di mantenere l'animale nella posizione corretta e modulare lo spettro neutronico per ottimizzare la distribuzione di dose nel tumore. All'interno di questo sitema è stata inserita una rappresentazione geometrica fortemente semplificata di un modello murino, caratterizzata dalla presenza di un tumore superficiale. Tale configurazione è stata adottata al fine di verificare la validità dell'approssimazione di equilibrio tra dose e KERMA nelle condizioni di interesse. Questa parte del lavoro è servita per verificare la possibilità di condurre in seguito simulazioni analoghe a quelle condotte per i pazienti umani, per i quali si opera in approssimazione di equilibrio di particelle cariche. A questo scopo, è stata inizialmente impiegata una sorgente neutronica estremamente semplificata. Successivamente, il modello è stato raffinato introducendo condizioni più realistiche: in primo luogo, uno spettro energetico identico a quello della sorgente neutronica ANTHEM, con neutroni collimati all'interno di un cono di apertura di 20°; in seguito, la sorgente ANTHEM completa, con lo spettro doppio-differenziale tipico di una sorgente reale. Questo approccio ha permesso di valutare le differenze tra le varie configurazioni e di stimare l'errore massimo associato all'adozione dell'approssimazione di equilibrio e all'uso dei fattori di KERMA. In una seconda fase, è stato implementato un modello murino voxelizzato derivato da immagini micro-CT, al fine di ottenere una rappresentazione anatomicamente realistica per le valutazioni dosimetriche. Sono stati quindi analizzati due casi studio rappresentativi: un tumore intracranico, modellante un Glioblastoma Multiforme, e un tumore superficiale sottocutaneo, rappresentativo di neoplasie del distretto testa-collo. Per ciascun caso, il trattamento è stato pianificato sulla base dei vincoli dosimetrici specifici dell'organo a rischio individuato, adottando limiti e criteri derivati dalla letteratura di riferimento nel contesto dei trials clinici di BNCT. Le distribuzioni di dose sono state quindi analizzate utilizzando sia il modello di dose pesata con fattori RBE fissi sia il modello di dose isoeffettiva a fotoni. Il confronto tra i due approcci ha evidenziato come il modello *RBE-weighted*, comunemente adottato in ambito clinico e radiobiologico, tenda a sovrastimare la dose equivalente nel tumore, risultando quindi non adeguato a descrivere in modo realistico gli effetti biologici della BNCT. I risultati evidenziano la capacità del codice IT_STARTS di fornire una descrizione dettagliata e quantitativa dello scenario di irraggiamento, includendo la distribuzione spaziale delle diverse componenti di dose e il loro impatto radiobiologico. Inoltre, l'utilizzo di un modello voxelizzato realistico consente di identificare organi critici che non emergerebbero in geometrie semplificate, migliorando l'affidabilità degli studi dosimetrici preclinici. Il presente lavoro rappresenta un passo preliminare verso esperimenti in vivo di BNCT su modelli animali, supportando la progettazione e l'ottimizzazione dei setup di irraggiamento, inclusi *holder* dedicati per piccoli animali. Sebbene non sia stato possibile includere i risultati relativi alla sorgente neutronica finlandese, la metodologia sviluppata verrà

applicata in future campagne sperimentali, consentendo un confronto coerente tra diverse facility, tra cui il centro BNCT di Helsinki e il centro ANTHEM di Caserta. Nel complesso, l'approccio proposto contribuisce a colmare il divario tra dosimetria computazionale e radiobiologia sperimentale in vivo, fornendo uno strumento utile per supportare la traslazione degli studi preclinici di BNCT verso applicazioni cliniche.

Abstract

This study investigates computational dosimetry applied to Boron Neutron Capture Therapy (BNCT) for in vivo radiobiological experiments, employing epithermal neutron sources produced by accelerator-based systems. These sources correspond to beams either already operational or currently under construction for clinical BNCT applications. The neutron sources referenced in this thesis are the clinical beam at Helsinki University Hospital, generated by the Neutron Therapeutics accelerator, and the clinical beam designed and under construction in Italy within the framework of the PNC-PNRR ANTHEM project. In the first phase of the work, a preliminary study of an irradiation holder for small animals was carried out, with the dual purpose of maintaining the animal in the correct position and modulating the neutron spectrum to optimize the dose distribution within the tumor. A highly simplified geometric representation of a murine model was incorporated into this system, featuring a superficial tumor. This configuration was adopted to verify the validity of the charged particle equilibrium approximation between absorbed dose and KERMA under the conditions of interest. This part of the work served to assess the feasibility of subsequently performing simulations analogous to those conducted for human patients, in which the charged particle equilibrium approximation is routinely assumed. To this end, an extremely simplified neutron source was initially employed. The model was then progressively refined by introducing increasingly realistic conditions: first, an energy spectrum identical to that of the ANTHEM neutron source, with neutrons collimated within a cone of 20° half-angle; subsequently, the full ANTHEM source, characterized by the double-differential spectrum typical of a real accelerator-based neutron beam. This approach enabled the assessment of differences among the various configurations and the estimation of the maximum error associated with the adoption of the equilibrium approximation and the use of KERMA factors. In the second phase, a voxelized murine model derived from micro-CT imaging was implemented in order to obtain an anatomically realistic representation for dosimetric evaluation. Two representative case studies were then analyzed: an intracranial tumor modelling a Glioblastoma Multiforme, and a superficial subcutaneous tumor representative of head and neck malignancies. For each case, the treatment was planned on the basis of the dosimetric constraints specific to the identified organ at risk, adopting limits and criteria derived from the reference literature in the context of BNCT clinical trials. The resulting dose distributions were analyzed using both the RBE-weighted dose model with fixed weighting factors and the photon isoeffective dose model. The comparison between the two approaches revealed that the *RBE-weighted* model, commonly adopted in clinical and radiobiological practice, tends to overestimate the equivalent dose in the tumor, and is therefore not adequate to realistically describe the biological effects of BNCT. The results demonstrate the capability of the IT_STARTS code to provide a detailed and quantitative description of the irradiation scenario, encompassing the spatial distribution of the individual dose components and their radiobiological impact. Furthermore, the use of a realistic voxelized model allows the identification of critical organs that would not emerge in simplified geometries, thereby improving the reliability of preclinical dosimetric studies. This work represents a preliminary step towards in vivo BNCT experiments on animal models, supporting the design and optimization of irradiation setups, including dedicated holders for small animals. Although it was not possible to include results pertaining to the Finnish neutron source, the methodology developed will be applied in future experimental campaigns, enabling a coherent comparison among different facilities, including the Helsinki BNCT center and the ANTHEM facility in Caserta. Overall, the proposed approach contributes to bridging the gap between computational dosimetry and experimental in vivo radiobiology, providing a valuable tool to support the translation of preclinical BNCT studies towards clinical applications.

Contents

Chapter 1

Introduction

1.1 Boron Neutron Capture Therapy

Neutron Capture Therapy (NCT) is a technique designed to selectively deliver high Linear Energy Transfer (LET) radiation from heavy charged particles directly to tumor cells. Among its variants, Boron Neutron Capture Therapy (BNCT) combines an external beam of low-energy neutrons ($E < 0.5$ eV) with a ^{10}B-containing pharmaceutical that is preferentially concentrated in tumor tissue. The underlying nuclear reaction, illustrated in Figure 1.1, exploits the exceptionally high neutron capture cross-section of ^{10}B ($\sigma = 3840$ barns at 0.025 eV), which surpasses that of all other elements present in biological tissue at thermal neutron energies. Upon neutron capture an alpha particle and a recoiling ^{7}Li nucleus are produced, both of which deposit their energy with high spatial localization within the tumor cell [1].

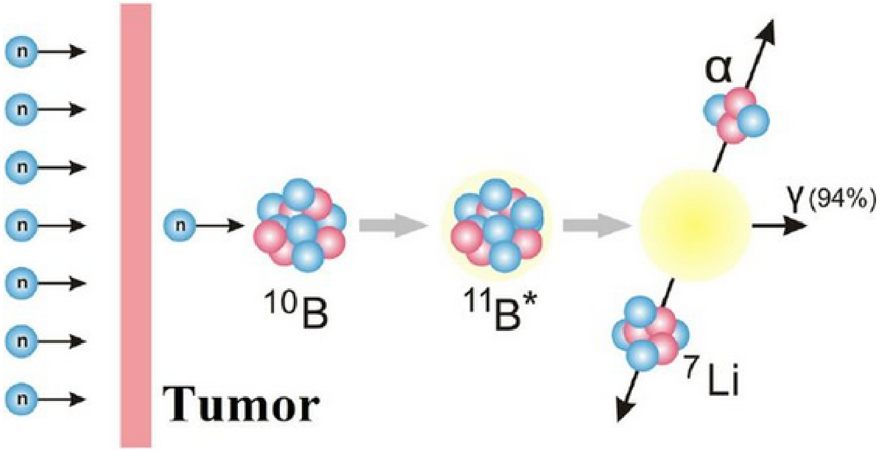

Figure 1.1: BNCT nuclear reaction. Illustration from [2]

The therapeutic potential of BNCT is closely tied to the physical properties of these reaction products. Both are high-LET particles: 164 keV μm^{-1} for the α particle and 151 keV μm^{-1} for the ^{7}Li nucleus, meaning that they release their energy over a very short distance [1]. In fact, the range of α particles in biological tissue is approximately 9 μm, while that of ^{7}Li nuclei is about 5 μm. Since a typical cell diameter is of the order of 10 μm, the entire energy of the reaction products is deposited within the cell in which the reaction occurs, in close proximity to the DNA: the primary target in cancer treatment. This combination of nuclear and biological selectivity gives BNCT a distinctive advantage over conventional radiation therapies. As a form of nuclear medicine, BNCT relies on biochemical rather than geometric targeting, making it ideally suited for treating spread tumours, infiltrations and undetectable micrometastases while minimizing damage to surrounding healthy tissue. To achieve selectivity, BNCT protocols are designed to maximize the boron-specific radiation component delivered to the tumor and to minimize the non-selective background dose, by using a tumour-specific drug able to guarantee a suitable tumour-to-normal tissue boron concentration ratio. Furthermore, since dose deposition depends primarily on boron localization rather than on beam geometry, BNCT is less sensitive to organ motion than other particle therapies and the Planning Target Volume (PTV) can be expanded to encompass potentially undetectable tumor cells beyond the gross tumor margin. From a clinical perspective, BNCT is a non-mutilating, organ-preserving treatment that is typically administered in a single session (or at most two) while maintaining therapeutic efficacy and toxicity comparable to standard radiotherapy, thus contributing to an improved quality of life for the patient. As mentioned, selectivity and effectiveness of BNCT ultimately depend on the ability to achieve a sufficiently high ^{10}B concentration in the tumor relative to healthy tissues, which represents its most fundamental distinction from conventional external beam radiotherapy. To this end, boron carriers must satisfy three key requirements:

- have a low toxicity;
- have a high capacity to be absorbed by malignant tissues and low penetration in the healthy ones;
- be expelled relatively quickly from blood and normal tissues, while persisting in tumor for at least the duration of the irradiation.

The two boron compounds that have been used in clinical applications are BPA (Boronophenylalanine) and BSH (sodium borocaptate), with BPA being the one currently employed. BPA is a precursor of melanin and it was first used in the treatment of melanoma by Mishima et al. [3] [4], though its affinity for melanin also results in non-negligible uptake by normal skin. BPA is now an approved drug in Japan [5].

A fundamental component of any BNCT system is the neutron source, which can be provided either by research nuclear reactors or by particle accelerators. Nuclear reactors have been extensively used since the Sixties for BNCT clinical trials and some of them are still in operation with dedicated BNCT facilities [6]. However, research nuclear reactors are not medical devices and it is very difficult to establish routine clinical treatments in these installations. In recent years, the accelerator-based approach has gained considerable momentum, with facilities established at numerous sites worldwide thanks to the availability of technologies able to produce neutron beam of suitable intensity [7]. This is essential to guarantee a sufficient neutron flux to trigger enough nuclear reactions with boron in a reasonable treatment time [1]. Compared to reactor-based systems, this technology offers significant practical advantages, including reduced footprint, simplified licensing and easier operation and maintenance, making hospital-based installation feasible.

Accelerator-Based BNCT (AB-BNCT) employs a proton or deuteron beam impinging on suitable targets to generate neutrons through reactions such as ^{7}Li(p,n)^{7}Be or ^{9}Be(d,n)^{10}B. The neutrons produced at the target are subsequently moderated to form clinical beams of two types, distinguished by their mean energy: thermal (25 meV) and epithermal (0.1 eV $< E_n <$ 100 keV). Thermal beams are suited for superficial tumors such as skin melanoma, while epithermal beams are designed to produce a uniform thermal neutron distribution at greater tissue depths, enabling the treatment of deep-seated tumors [1].

In the next Section, the two accelerator-based neutron sources relevant for this thesis are briefly introduced.

1.2 The two facilities and the neutron sources

1.2.1 Finnish facility

Helsinki University Hospital, in collaboration with Neutron Therapeutics, Inc. (Danvers, MA, USA), initiated a joint project in 2016 to install a compact accelerator-based neutron source on the hospital campus. The design and construction of the facility followed international recommendations for BNCT centers [1]. The building is situated adjacent to the cancer clinic of the hospital and it is connected to its main infrastructure via a service tunnel, allowing immediate access to clinical resources required for BNCT treatments. The facility layout is shown in Figure 1.2.

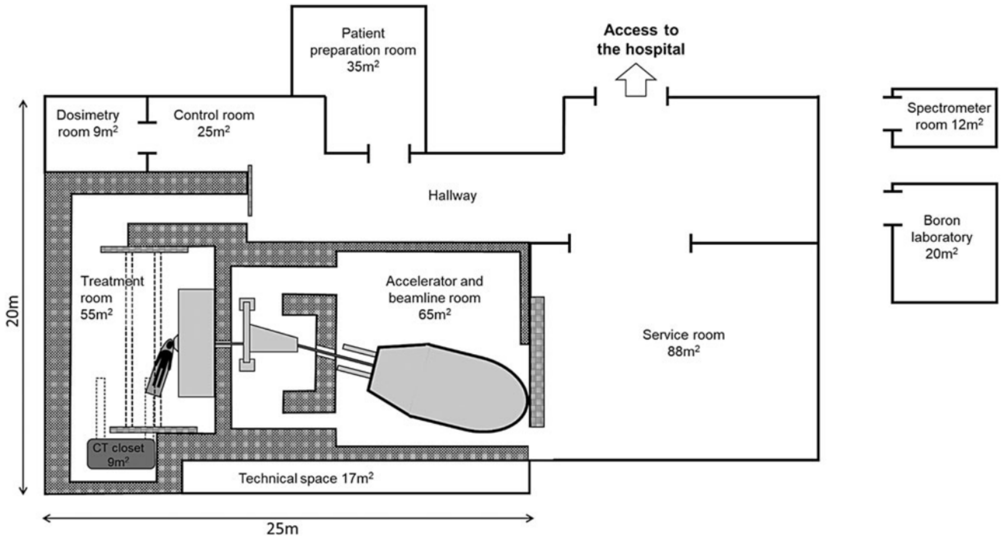

Figure 1.2: The layout of the Finnish BNCT facility equipped with the NuBeam neutron source.

The treatment room is shielded with thick heavy concrete walls lined with borated or lithiated plastic to enhance neutron absorption. Patient positioning for irradiation is achieved using a six-degree-of-freedom robotic image-guided positioning system (Exacure®, BEC GmbH, Reutlingen, Germany). In-room imaging is performed with a rail-mounted Somatom Confidence RT

CT scanner (Siemens Healthineers, Erlangen, Germany), which remains shielded during neutron irradiation. On the day of treatment, the patient is placed on the robotic couch using a custom-made immobilization mask and vacuum cushions prepared in advance. The positioning system automatically aligns the patient with the pre-treatment planning CT and/or MRI images and the robotic couch then moves the patient precisely into the irradiation position. The NuBeam system (Neutron Therapeutics, Inc.) consists of a proton accelerator coupled with a lithium target that converts the proton beam into neutrons. The accelerator is a single-ended electrostatic Cockcroft–Walton-type machine operating at a proton energy of 2.6 MeV and a beam current of up to 30 mA. Neutron production occurs within an optimized Beam Shaping Assembly (BSA) located inside the treatment room. In the BSA, the proton beam is directed onto a cooled, rotating solid lithium target, generating low-energy neutrons through the p–Li reaction. Neutrons thus generated then pass through an optimized moderator to shape the desired therapeutic spectrum: this is the Beam Shaping Assembly (BSA) the typical structure of the facility that tailors the spectral characteristics and the collimation of the neutron beam to optimize the clinical effectiveness. The neutron beam was designed in accordance with the recommendations outlined in the International Atomic Energy Agency (IAEA) TECDOC 1223 [1] and to closely reproduce the beam spectrum previously used at the FiR-1 reactor, which was employed in Finland for BNCT treatments until its closure in 2012 [8]. Beam monitoring is performed using two neutron detectors and one gamma detector positioned near the beam exit port. Circular beam collimators made of enriched ^{6}Li polyethylene are used, offering aperture diameters identical to those previously available at the FiR-1 facility (8, 11, 14, 17 and 20 cm) [9].

1.2.2 Italian facility

The ANTHEM project (AdvaNced Technologies for Human-centrEd Medicine) is funded by the National Plan for NRRP Complementary Investments (PNC), within the call supporting research initiatives focused on innovative technologies and new therapeutic pathways in the health and care sectors. The project is structured into four thematic Spokes, each addressing a specific research domain:

- Spoke 1 "Data and technology driven diagnosis and therapies";
- Spoke 2 "Connecting patients and therapists through adaptive environments and intelligent sensors to enhance proximity medicine";
- Spoke 3 "Risk factors monitoring, diagnostic tools and therapies in chronic disease";
- Spoke 4 "Preclinical and clinical breakthrough theranostic and treatments for cancer".

Each Spoke is further organized into Pilots dedicated to specific objectives. Within Spoke 4, Pilot 9 focuses on the development of a new facility for Boron Neutron Capture Therapy (BNCT) research and clinical application in Caserta, at the University of Campania “Luigi Vanvitelli”. The neutron beam production system is designed and constructed by the National Institute for Nuclear Physics (INFN) [10]. The technology is based on a proton accelerator coupled to a beryllium target and a BSA. The accelerator, developed at the National Laboratories of Legnaro (LNL), consists of a Radio Frequency Quadrupole (RFQ) capable of delivering a continuous-wave proton beam with an energy of 5 MeV and a current of 30 mA [11]. The accelerator has been constructed, tested, aligned with a precision of 30 μm and resonantly coupled. The final cleaning is completed and assembly is ongoing. The proton beam impinges on a Be-Pa-Cu target, also designed at LNL and currently in its prototypal phase. The BSA, developed in Pavia, is designed to properly tailor the neutron energy spectrum and beam collimation for clinical use [12]. An innovative optimization methodology is employed to identify the most suitable material configuration and to assess the therapeutic performance of the beam. A preliminary version of the BSA design is presented in the referenced publication; however, subsequent modifications to the target design and practical construction constraints required a revision and structural simplification of the assembly. The updated BSA configuration is expected to provide a neutron flux at the beam port higher than $10^9 cm^{-2} s^{-1}$, in accordance with clinical guidelines, starting from a neutron production rate of approximately $10^{14} s^{-1}$ at the target. Pilot 4.9 also includes the architectural design and construction of the building hosting the BNCT facility.

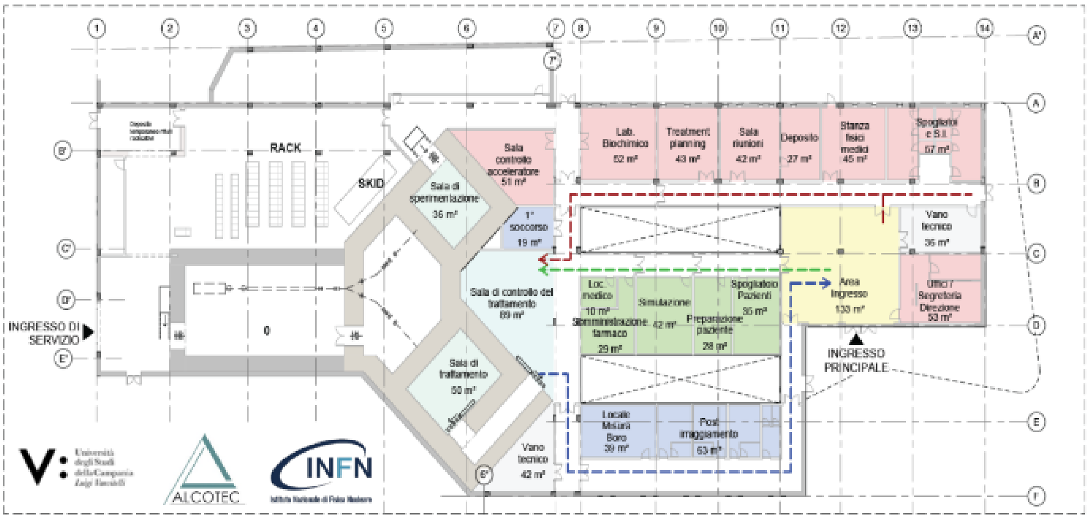

Figure 1.3: Building plan of ANTHEM project facility for BNCT in Caserta.

The structure, as shown in the Fig.1.3, comprises areas dedicated to the neutron production technology, a treatment irradiation room for patients, an additional irradiation room for experimental activities and clinical and research spaces for patients and staff. The right-hand section includes rooms designated for patient reception and preparation, including boron administration and positioning in a preparation room geometrically consistent with the irradiation room. This area also houses laboratories for boron concentration measurements and medical physics activities, as well as a recovery room for post-irradiation monitoring. The staff-related areas, including the hospital admission office, locker rooms, treatment planning rooms, biochemical laboratory and accelerator control room, are identified in pink in the layout. The patient pre-treatment areas, including changing rooms and drug administration spaces, are indicated in green. The post-treatment areas, shown in blue, are dedicated to final boron concentration assessments and clinical checks prior to discharge [13].

A detailed representation of the accelerator system and associated beam production components located in the building space is provided in Fig.1.4.

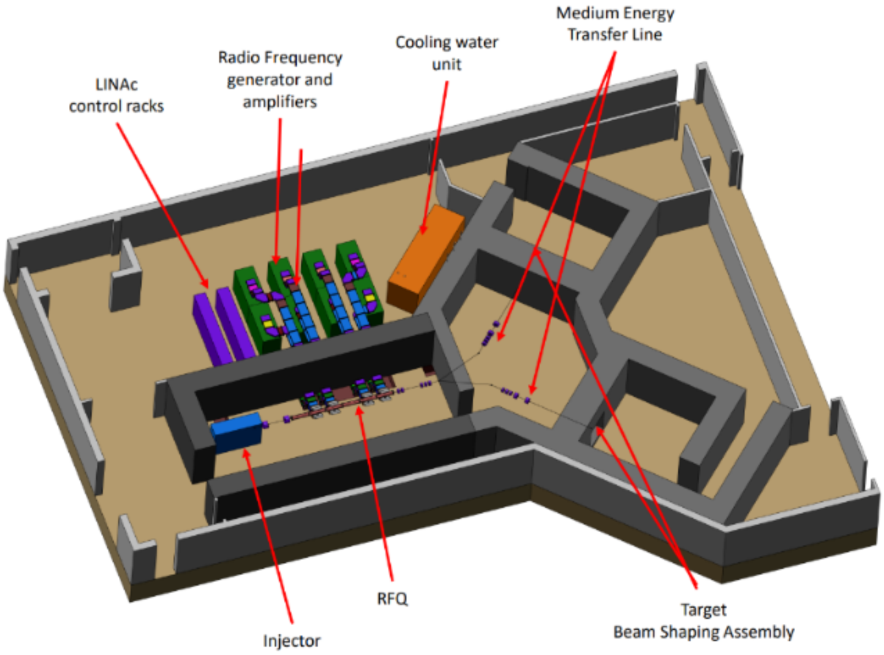

Figure 1.4: The structure of the building showing the areas dedicated to the accelerator and its technical ancillaries and the two irradiation rooms.

1.3 BNCT dosimetry

1.3.1 BNCT Dose Components

According to ICRU Report 44 [14], soft tissue is primarily composed of oxygen ^{16}O (76.2%), carbon ^{12}C (11.1%), hydrogen ^{1}H (10.1%) and nitrogen ^{14}N (2.6%) in atomic fraction. In the context of BNCT dosimetry, hydrogen and nitrogen play a central role in neutron interactions due to their comparatively large microscopic cross sections and significant KERMA factors. On the contrary, reactions involving oxygen and carbon produce dose contributions that are small enough to be neglected in first-order dosimetric assessments. Although the elastic scattering cross section of hydrogen is lower than its capture cross section, the associated dose contribution remains substantial because of its high abundance in biological tissue. In particular, recoil protons generated by neutron scattering above approximately 10 keV deposit a non-negligible high-LET dose component. During penetration into tissue, epithermal and fast neutrons progressively lose energy through elastic scattering, predominantly with hydrogen nuclei. In the $^{1}H(n,n')p$ interaction, the incident neutron transfers, on average, half of its kinetic energy to a recoil proton, which is characterized by relatively high LET. Thermal neutrons, instead, predominantly undergo capture reactions such as $^{1}H(n,\gamma)^{2}H$ and $^{14}N(n,p)^{14}C$. The hydrogen capture reaction produces a low-LET photon with energy $E_\gamma = 2.2$ MeV, whereas nitrogen capture releases a proton with intermediate LET and energy $E_p = 590$ keV [1].

For an epithermal neutron beam, the absorbed dose in BNCT can be thus decomposed into four principal components:

- D_B: boron dose component, originating from the high-LET charged particles produced by the $^{10}B(n,\alpha)^7Li$ reaction. This represents the therapeutically dominant contribution [15].
- D_{th}: thermal neutron dose component, arising from interactions of thermal neutrons ($E_{th} < 0.5$ eV) with tissue, primarily via the $^{14}N(n,p)^{14}C$ reaction.
- D_f: fast neutron dose component, associated with the moderation and thermalization of fast neutrons ($E_f > 10$ keV). Recoil protons produced through elastic scattering deposit significant dose, particularly at shallow depths, with an exponential decrease as neutrons slow down.
- D_γ: gamma dose component, delivered by photons produced through $^1H(n,\gamma)^2H$, the $^{10}B(n,\alpha)^7Li$ reaction and photons already present in the incident beam.

The total absorbed dose delivered by the mixed BNCT radiation field is therefore expressed as:

$$D = D_B + D_{th} + D_f + D_\gamma \tag{1.1}$$

Given this mixture of different radiation components, the radiobiological response to BNCT is inherently more complex than that of conventional photon radiotherapy, also due to the strong dependence of biological effectiveness on the microdistribution of boron within tissues. In fact, the spatial distribution of boron at the tissue, cellular and subcellular levels critically determines treatment effectiveness. Because α particles and ^{7}Li ions travel only a few micrometers, the biological effect depends not only on macroscopic boron concentration but also on its localization relative to radiosensitive targets such as DNA. This topic has been extensively studied in Pavia [16]. In addition, vascular dynamics, tumor microenvironment, hypoxia, immune response and intercellular signaling significantly modulate radiation response. These aspects cannot be reproduced adequately *in vitro*, making animal models essential for realistic radiobiological characterization.

Each radiation component of the BNCT field is characterized by distinct physical properties, LET distributions and biological effectiveness and exhibits spatial variation due to neutron moderation, attenuation and tissue composition [1]. Because each of these contribution cause different biological damages at the same absorbed dose, this quantity alone is insufficient to describe the effects in BNCT. Thus, absorbed dose is not a robust predictive tool to generate a desired clinical outcome of a BNCT treatment.

This is why clinical BNCT protocols require conversion of the absorbed dose into photon-equivalent quantities to enable comparison with conventional photon radiotherapy outcomes and to enable reliable dose prescriptions based on the large clinical experience gained in conventional photon therapy. A large variety of units to indicate the administered dose in photon equivalent units have been established by the BNCT community, such as Gy-Eq, Gy(RBE) and Gy(IsoE), depending on the adopted model [1]. The choice of the model to use for the translation is matter of active research. The first model employed since the Nineties is the one based on fixed Relative Biological Effectiveness (RBE) values [17].

1.3.2 The RBE-Weighted Dose Model

The RBE is defined as the ratio between the absorbed dose of a reference radiation (typically ^{60}Co γ-rays), D_R, and the absorbed dose D_X of the radiation under investigation that produces the same biological endpoint:

$$\frac{D_R}{D_X}. \tag{1.2}$$

RBE thus quantifies the relative effectiveness of a given radiation in producing a specified biological effect at a certain endpoint compared to photons. Typically, RBE is derived from *in vitro* radiobiological experiments, such as the measure of cell survival as a function of the dose. The chosen endpoint is, for example, a certain fixed percentage of cell survival. The RBE values can also be established in *in vivo* experiments, by fixing a certain effect evaluated in animals; this is especially done for the healthy tissues [17]. In the conventional approach, the absorbed BNCT dose is converted into a biologically weighted dose D_W by multiplying each component by a corresponding dose-independent RBE factor. For the boron component, the weighting factor also accounts for the microscopic distribution of boron at the cellular level. This parameter, known as Compound Biological Effectiveness (CBE), reflects not only LET dependence, but also the different effectiveness of a borated drug which depends on intracellular localization.

The weighted BNCT dose is thus calculated as:

$$D_W = CBE \cdot D_B + RBE_{th} \cdot D_{th} + RBE_f \cdot D_f + RBE_\gamma \cdot D_\gamma \tag{1.3}$$

Although this model has historically been employed in clinical BNCT applications, it presents intrinsic limitations. In particular, the assumption of fixed, dose-independent weighting factors leads to inconsistencies when translating BNCT doses into photon-equivalent units [18]. The cited paper demonstrates how this approach is mathematically inconsistent and leads to a substantial overestimation of photon-equivalent doses, especially in the tumor, thereby reducing its predictive reliability.

1.3.3 The Photon-Isoeffective Dose Model

To overcome these limitations, the photon-isoeffective dose model was proposed [18]. The photon isoeffective dose is defined as the dose of the reference radiation (photons) which gives the same effect as the dose of BNCT. Unlike the fixed RBE approach, this formalism is based on the complete cell survival curve (or the curve of the effect measured as a function of the dose in the radiobiological experiment) and it does not fix an arbitrary endpoint. In case of survival curves, the model also incorporates sublethal damage repair and synergistic interactions between radiation components. This is important because the BNCT irradiation is typically longer than the repair time of tumor cells and thus the repair plays a role in the tumor control. Moreover, synergism may arise from different sub-lethal damages caused by different radiation components.

Within the Linear-Quadratic (LQ) formalism, cell survival is expressed as:

$$S(D) = e^{-(\alpha D + \beta D^2)} \tag{1.4}$$

where α represents damage from single events and β represents damage from pairwise interactions of sublesions.

To account for first-order repair processes, the quadratic term is modulated by the generalized Lea-Catcheside factor $G(\theta)$:

$$S(D) = e^{-(\alpha D + G(\theta)\beta D^2)} \tag{1.5}$$

The time-dependent repair factor considering fast and slow kinetics is written as:

$$G_i(\theta, t_{0f}, t_{0s}) = p_{if} G(\theta, t_{0f}) + p_{is} G(\theta, t_{0s}) \tag{1.6}$$

with

$$G(\theta, t_0) = \frac{2t_0}{\theta}\left[1 - \frac{t_0}{\theta}(1 - e^{-\frac{t_0}{\theta}})\right] \tag{1.7}$$

The independent action case leads to:

$$S(D_1, ..., D_4) = \prod_{i=1}^{4} S_i(D_i) \tag{1.8}$$

and

$$-\ln(S_R(D_R)) = \sum_{i=1}^{4} \alpha_i D_i + G_4(\theta)\beta_4 D_4^2 \tag{1.9}$$

which ultimately yields the photon-isoeffective dose:

$$D_R(D_1, ..., D_4) = \frac{1}{2}\frac{(\frac{\alpha}{\beta})_R}{G_R}\left[\sqrt{1 + \frac{4G_R}{\alpha_R(\frac{\alpha}{\beta})_R}\left(\sum_{i=1}^{4} \alpha_i D_i + G_4(\theta)\beta_4 D_4^2\right)} - 1\right] \tag{1.10}$$

When synergistic interactions between radiation components are considered, additional quadratic cross-terms appear:

$$-\ln(S(D_1, ..., D_4)) = \sum_{i=1}^{4} \alpha_i D_i + \sum_{i=1}^{4}\sum_{j=1}^{4} G_{ij}(\theta)\sqrt{\beta_i\beta_j} D_i D_j \tag{1.11}$$

leading to the generalized photon-isoeffective dose:

$$D_R(D_1, ..., D_4) = \frac{1}{2}\frac{(\frac{\alpha}{\beta})_R}{G_R}\left[\sqrt{1 + \frac{4G_R}{\alpha_R(\frac{\alpha}{\beta})_R}\left(\sum_{i=1}^{4}\alpha_i D_i + \sum_{i=1}^{4}\sum_{j=1}^{4} G_{ij}(\theta)\sqrt{\beta_i\beta_j}D_iD_j\right)} - 1\right] \tag{1.12}$$

Comparisons have demonstrated that photon-isoeffective dose values are systematically lower than those obtained with the fixed RBE model for absorbed dose values typical of tumors, and that these better correlate with observed tumor control probabilities. This confirms that the fixed RBE-weighted formalism is inadequate for predicting clinical outcomes, whereas the photon-isoeffective approach provides a biologically consistent translation of BNCT mixed-field doses into photon-equivalent values [19].

While in vitro radiobiological experiments provide a controlled and reproducible framework for deriving the parameters of the photon isoeffective dose model, they present inherent limitations that may compromise the clinical relevance of the resulting predictions. As discussed by Perotti Bernardini et al. [20], in vitro and in vivo radiobiological data yield photon isoeffective doses that differ by approximately 8-16% for typical clinical absorbed doses of 10-15 Gy, with discrepancies growing up to 30% at higher dose levels. More fundamentally, in vivo cancer models better mimic the complex biological environment of a tumor, including cell–cell and cell-matrix interactions, the vascular system and the heterogeneous spatial distribution of oxygen and nutrients, all of which play a pivotal role in determining the overall tumor response to radiation. Furthermore, the endpoint assessed in vivo, typically tumor complete response, is directly comparable to the clinical outcome used to evaluate the success of radiation therapy in patients, whereas clonogenic cell survival measured in vitro captures only one aspect of the overall biological response. This is even more significant for the evaluation of effects on healthy tissues, that are not only linked to the cell death.

The necessity of in vivo radiobiological experiments, motivate the simulation of these set-ups, able to calculate the absorbed dose in the tumor and in the surrounding healthy tissues in the animal models. In the context of BNCT, it is particularly interesting to derive the radiobiological parameters for the dosimetric models from in vivo experiments, requiring the calculation of precise dose maps in relevant volumes. Monte Carlo transport codes are the gold standard for this purpose, as they allow a detailed particle-by-particle simulation of neutron and photon interactions in complex heterogeneous geometries, providing accurate estimates of the KERMA/dose components for each radiation type at any point within the irradiated volume.

The availability of precise absorbed dose distributions in both the tumor and the healthy tissues of a computational model representative of the animal used in the radiobiological experiment enables the application of the photon isoeffective dose formalism to the experimental setting, making it possible to perform a full treatment planning for the radiobiological experiment itself. This approach opens the possibility of evaluating dose-response relationships, tumor control probabilities and normal-tissue complication probabilities strengthening the translational value of the preclinical data. Clearly, carrying out this type of analysis requires dedicated computational tools, in particular a Treatment Planning System, capable of handling Monte Carlo-based dose calculations, particle transport in biological geometries, calculation of relevant figures of merit and the implementation of radiobiological models (see next Chapters). Before deepening these aspects, this Chapter also introduces the relevant theoretical framework for the absorbed dose calculation in the models.

1.4 Charged-Particle and Radiation Equilibrium

The concepts of Radiation Equilibrium (RE) and Charged-Particle Equilibrium (CPE) play a fundamental role in radiological physics because they establish rigorous relationships between absorbed dose (the energy deposited in the volume per unit mass) and KERMA, which is the expectation value of the energy transferred to the charged particles per unit mass around the point of interest, including the energy that could be dissipated in radiative losses. These equilibrium conditions allow one to relate measurable quantities to transport-based physical quantities under well-defined geometrical and physical assumptions [21]. In fact, while the radiobiological relevant quantity is the absorbed dose, KERMA is more straightforward to calculate, requiring only the knowledge of the primary irradiation field in the volume of interest and the availability of tabulated KERMA factors. In some cases, it is possible to use KERMA as an approximation of the dose, being numerical equal under certain conditions.

1.4.1 Radiation Equilibrium (RE)

Radiation equilibrium (RE) exists within a volume V when, for each type and energy of radiation entering the volume, an identical radiation component leaves it. Under non-stochastic conditions, this requires:

- an homogeneous medium in terms of atomic composition and density;
- a uniformly distributed radioactive source;
- and the absence of inhomogeneous electric or magnetic fields capable of perturbing charged-particle trajectories.

RE is particularly relevant when the characteristic ranges of all primary and secondary radiations are small compared to the dimensions of the region of interest. Under these conditions, the energy transported into the volume is balanced by the energy leaving it, resulting in zero net energy flow across its boundary. Consequently, the absorbed dose equals the KERMA and can be evaluated solely from the energy released locally within the volume. In this case:

$$D = \frac{d\bar{\varepsilon}}{dm} \tag{1.13}$$

where $\bar{\varepsilon}$ denotes the expectation value of the energy imparted [21].

1.4.2 Charged-Particle Equilibrium (CPE)

Charged-particle equilibrium exists when every charged particle of a given type and energy leaving a volume is replaced by an identical one entering it. Radiation equilibrium is a sufficient condition for CPE, but not a necessary one. In practice, CPE may exist even when RE does not.

The practical importance of CPE lies in the fundamental relationship:

$$D = K_c \tag{1.14}$$

meaning that under CPE conditions the absorbed dose equals the collision KERMA at that point, being this the energy per unit mass, transferred to secondary particles which will be dissipated by collisions. This equality holds independently of radiative losses, provided that the volume considered is infinitesimal so that bremsstrahlung photons escape. In the presence of indirectly ionizing radiation (photons or neutrons), if the medium is homogeneous and the radiation field is spatially uniform, secondary charged particles are produced uniformly throughout the region. Although their angular distribution may be anisotropic, homogeneity ensures reciprocity of particle transport, thus establishing CPE even without radiation equilibrium. This principle underlies the operation of ionization chambers and the measurement of exposure, since exposure measurement depends on achieving CPE in air [21].

Failure of CPE

CPE fails when the symmetry of charged-particle transport is broken. The main causes include:

- Proximity to a radiation source (spatially non-uniform fluence),
- Proximity to a boundary between media of different density or composition,
- High-energy radiation where secondary particle range becomes comparable to or larger than attenuation length,
- Presence of non-uniform electromagnetic fields.

A representative example is the dose buildup region near the surface of a phantom/tissue irradiated by radiotherapy photon beams. Because secondary electrons have a finite range, at shallow depths there are fewer electrons entering the point than leaving it. As depth increases, electron population builds up until a near-equilibrium condition is approached. At very high photon energies, the attenuation length of primary radiation becomes comparable to or larger than the range of secondary electrons, producing intrinsic CPE failure even in homogeneous media [21].

1.4.3 Transient Charged-Particle Equilibrium (TCPE)

When full CPE is not achieved but absorbed dose remains proportional to collision KERMA, the condition is termed Transient Charged-Particle Equilibrium (TCPE). In TCPE:

$$D = K_c\, f(x) \tag{1.15}$$

where the proportionality factor exceeds unity and depends on depth and transport geometry. In broad beams of high-energy photons incident on a slab, the dose increases with depth near the surface due to electron buildup, reaches a maximum (D_{max}), and then decreases approximately in parallel with the collision KERMA curve. Beyond the buildup region, although strict CPE is not satisfied, dose remains proportional to K_c, defining TCPE.

Mathematically, under TCPE conditions:

$$D = K_c e^{\mu' x} \tag{1.16}$$

where μ' is the effective attenuation coefficient and x is the mean forward range of secondary charged particles. This relationship allows dose to be related to KERMA even when full equilibrium is not achieved. TCPE is particularly relevant for megavoltage photon beams in radiotherapy and provides the theoretical framework allowing exposure and dose relationships to remain meaningful at high energies, despite the breakdown of strict CPE.

In summary, RE ensures complete balance of all radiations, CPE ensures charged-particle balance and leads to the fundamental equality $D = K_c$, and TCPE describes high-energy situations in which dose remains proportional to collision KERMA despite the absence of full equilibrium. These concepts are central to understanding dose deposition, exposure measurement and the interpretation of dosimetric quantities in clinical and experimental radiation physics [21].

1.5 Treatment Planning

In radiotherapy, treatment planning refers to the procedure through which a specialized team, including the radiologist, the radiation oncologist and the medical physicist, defines the most appropriate irradiation set-up for a patient diagnosed with a tumor. The choice of patient positioning and beam arrangement must be carefully optimized to deliver a sufficient therapeutic dose to the target region while keeping the dose to healthy surrounding tissues as low as possible [22]. The most important steps in the development of a treatment plan are:

- Collecting of patient data, typically through CT or MRI imaging.
- Delineation of tumor volumes and identification of organs at risk.
- Development of a computational model of the patient and the radiation source.
- Evaluation of the absorbed dose distribution for varying patient setups and beam arrangements.
- Determination of the correct patient positioning during treatment delivery.

1.5.1 Volume Definition

A fundamental step in treatment planning is the definition of the tumor volumes, as described in ICRU Reports 50 [23] and 62 [24] and the identification of the organs at risk [25].

- Gross Tumor Volume (GTV): the portion of the tumor that is macroscopically detectable and localized through diagnostic imaging (CT, MRI etc.), physical examination or laboratory investigations including histological and pathological assessments.
- Clinical Target Volume (CTV): a volume that includes the GTV and any subclinical microscopic disease requiring therapeutic irradiation. It may be obtained by applying a uniform or non-uniform geometric expansion to the GTV (e.g. GTV $+$ 1 cm) or it may overlap entirely with the GTV. Several distinct, non-adjacent CTVs may be defined when different dose levels are prescribed to different disease sites.

- Internal Target Volume (ITV): an intermediate volume designed to incorporate the expected range of positional and morphological variations of the CTV with respect to the patient's anatomical reference system (usually the skeletal structure), caused by involuntary physiological processes such as breathing or organ motion related to bladder and rectal volume changes.
- Planning Tumor Volume (PTV): a purely geometric construct that provides an additional margin around the CTV to guarantee that the prescribed dose is reliably delivered, compensating for residual uncertainties in beam delivery reproducibility and equipment mechanical tolerances.

The relationship among these volumes is schematically represented in Figure 1.5.

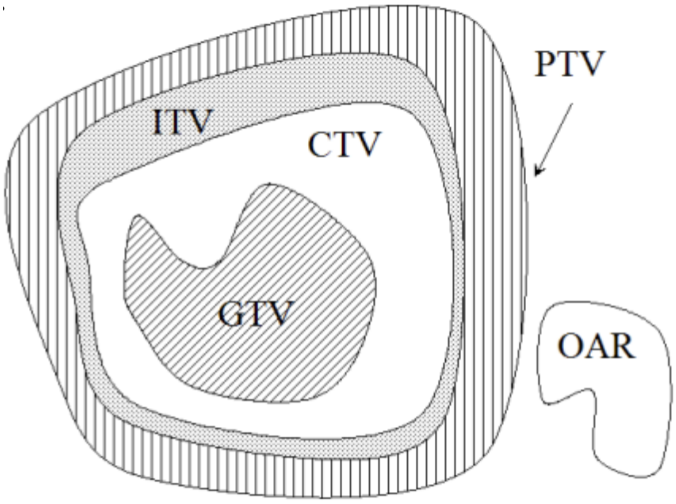

Figure 1.5: Representation of the tumor volumes [22].

Special consideration must be devoted to the organs at risk (OARs), defined as anatomical structures exhibiting limited radiation tolerance. In some cases, the tumor may be entirely embedded within an organ at risk , as is the case for glioblastoma multiforme, one of the tumor models simulated in this study, which develops within the brain tissue itself. When such structures lie in close proximity to, or directly encompass, the tumor, it may be necessary to adjust the beam incidence angles or revise the prescribed dose levels accordingly. Furthermore, even OARs located at a greater distance from the target must be carefully monitored, as exposure beyond their tolerance limits, even in the absence of direct overlap with the treatment field, may result in serious and potentially irreversible clinical complications.

1.5.2 BNCT Treatment Planning

In current clinical practice, the optimization of treatment plans for conventional photon-based radiotherapy relies on analytical algorithms that enable fast and accurate computation of the dose delivered to the patient. In the context of BNCT, however, the stochastic nature of neutron interactions with matter makes such analytical approaches impossible, and Monte Carlo methods must be employed instead. The following sections outline the most relevant steps involved in the construction of a BNCT treatment plan [26].

Patient modeling

Treatment planning simulation begins with the generation of a three-dimensional anatomical model of the patient, derived from CT or MRI acquisitions. This model provides the geometric framework within which radiation transport calculations are performed, generally using Monte Carlo transport codes such as MCNP [27] or PHITS [28]. For this purpose, the treatment planning software must be able to translate medical imaging data into a geometry input file formatted according to the requirements of the selected Monte Carlo code. A number of modelling strategies have been developed over the years, among which the voxel model, the univoxel model and the NURBS representation are the most notable. The present work focuses exclusively on the voxel model, as it constitutes the modelling approach adopted throughout this study.

Voxel model

Among the available approaches, the voxel model is both the most straightforward and the most commonly employed in clinical and research settings. The patient volume is discretized into a regular three-dimensional grid of contiguous rectangular elements, known as the voxels, each characterized by a homogeneous tissue composition and typical dimensions between 2 and 10 mm per side. Due to computational constraints, the number of distinct tissue types that can be modeled simultaneously is limited, restricting the range of assignable material combinations (Figure 1.6). Adopting coarse voxel sizes risks producing an inaccurate anatomical representation, especially near curved or irregular tissue boundaries. While finer voxels improve geometric fidelity, the associated increase in computation time is often mitigated by selecting a scoring mesh with a resolution lower than that of the voxel grid, which however reduces the practical benefit of the finer discretization. A viable solution to this trade-off is the multi-voxel strategy, in which the spatial resolution is locally adapted to the dosimetric complexity of the region: fine voxels are placed where dose gradients are steep or where different tissue types are in contact, whereas coarser voxels are used in large, uniform regions where high resolution is unnecessary [29, 30]. With the computational resources available at the present day, also a uniform voxelization with very small voxel dimension is feasible, making the algorithm for the transformation of the medical images into a Monte Carlo model more straightforward. In the present work, moreover, the small physical dimensions of the murine model under investigation required a uniformly fine voxel resolution to be maintained throughout the entire volume. This was possible without incurring prohibitive computational costs.

Tissue composition and boron concentration

In contrast to conventional photon or electron radiotherapy, where dose computation is largely based on the electron density map extracted from CT data, BNCT demands a detailed specification of the elemental composition of each tissue type. This requirement arises from the strong dependence of neutron interaction cross-sections on the chemical constituents of the irradiated medium, which vary considerably across different biological tissues. Among all elements present

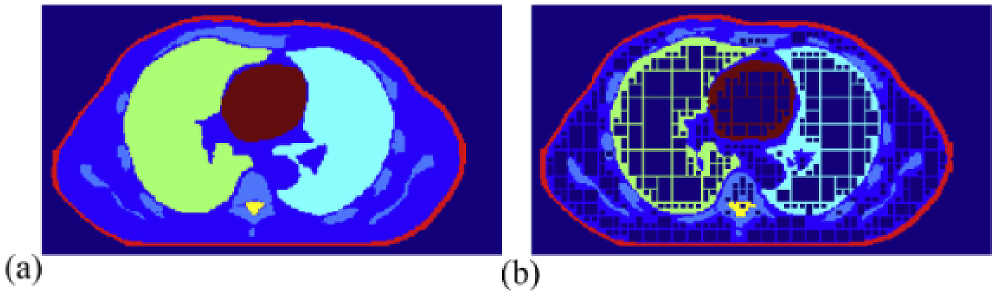

Figure 1.6: (a) Volumes of Interest marked for reconstruction in a coronal view of the human thorax and (b) corresponding MultiCell-based model for MCNP. Illustration from [30].

in the human body, hydrogen and nitrogen exert the greatest influence on neutron transport and dose deposition, owing to both their relatively high concentrations in tissue and the sizeable magnitude of their respective neutron cross-sections. In addition, an accurate definition of the boron concentration specification is important in both the tumor and the surrounding healthy tissue since the large neutron capture cross-section of ^{10}B perturbs the local neutron flux and therefore has a non-negligible effect on the resulting dose distribution throughout the patient volume[1].

Dose prescription

While in conventional external beam radiotherapy the clinician directly prescribes the dose to be administered to the tumor or to the planning target volume, dose prescription in BNCT involves a substantially greater degree of complexity. On one hand, the inherent difficulty of converting a mixed radiation field into photon-equivalent units makes the precise determination of the therapeutic dose at the tumor site even more difficult, as there is still a debate on the real equivalence of BNCT dose to photon units. Thus, the prescribed dose in BNCT is not defined in terms of tumor coverage, but is instead constrained by the radiation tolerance of the most radiosensitive normal tissue within the beam path, to guarantee a safe treatment leveraging on differential boron uptake in tumor for the delivery of a therapeutic dose to the malignancy. In literature, dose constraints are often expressed in terms of photon-equivalent dose, calculated using fixed RBE values. While this model does not strictly correspond to the photon-isoeffective one [18], the discrepancy between the two becomes negligible at the low dose levels, typical of healthy tissues [31], as demonstrated in many clinical trials so far. The choice of the dose-limiting organ depends on the anatomical site of the tumor: structures, in particular for this study the brain and the mucosa, have been employed as reference organs at risk. Some protocols have adopted the mean dose to a specific organ, most commonly the brain, as the dose constraint, while others have simultaneously enforced limits on both the mean and the maximum dose. In the Finnish clinical trial for head and neck cancer, the irradiation time was specifically chosen to deliver a maximum absorbed dose of 6 Gy (absorbed dose) to the mucosa [8], instead for the brain in the Chinese and Taiwan clinical trials the irradiation time was chosen to deliver a mean weighted dose of 2.5 Gy and a maximum weighted dose of 13 Gy [6].

From a computational standpoint, the Monte Carlo simulation produces a three-dimensional dose rate map expressed in Gy/s, defined over a scoring grid overlaid on the patient geometry. Given a selected dose-limiting criterion, a threshold that can be for example on the peak mucosa dose or on the mean brain dose, the treatment planning software determines the irradiation time at which that threshold is reached. All dosimetric quantities are subsequently rescaled to this reference time, and the global dose distribution is characterized through meaningful figures such as the Dose Volume Histograms and the isodose curves distribution. Depending on the availability of models and parameters for the tumor and tissues under study, the treatment planning also allows to establish radiobiological figures of merit more related to the clinical outcome, such as the Tumor Control Probability or the Normal Tissue Complication Probability [32, 33].

This thesis addresses the preparation of *in vivo* radiobiological studies for BNCt of brain tumors, in particular of glioblastoma multiforme, and of head and neck recurrent or local-advanced cancer. The next two paragraphs briefly summarize the status of BNCT clinical applications of these two malignancies

1.5.3 BNCT for Glioblastoma Multiforme

Glioblastoma multiforme (GBM) is classified as a grade IV glioma by the World Health Organization (WHO), and it represents the most prevalent malignant brain tumor among the adult population. The National Cancer Institute reported roughly 23820 newly diagnosed cases of malignant brain tumors in the United States in 2019 alone, underscoring the significant clinical burden of this disease. Within the broader category of central nervous system neoplasms, gliomas represent 32% of all primary tumours, with glioblastomas and astrocytic tumours accounting for 28% and 17% of these, respectively. From a histopathological standpoint, GBM is a neuroepithelial malignancy originating from glial cells of the central nervous system. Several distinct histological subtypes have been identified within the glioma family, namely astrocytoma, oligodendroglioma and oligo-astrocytoma, each deriving from a different cellular precursor: astrocytes, oligodendrocytes and neuronal cells, respectively. The WHO grading system classifies gliomas on a scale from grade I to grade IV according to their histopathological characteristics, while the classification of GBM is further refined through molecular and genetic profiling, which can inform prognostic assessments and guide the design of individualized treatment strategies. The current therapeutic approach for GBM combines conventional radiotherapy with concomitant Temozolomide chemotherapy and, whenever surgically feasible, tumor resection. Despite ongoing progress in treatment protocols, patient prognosis remains dismal, with a median survival of approximately 14 months even under active treatment. Although GBM has been the subject of intensive research efforts over recent decades, no meaningful improvement in median overall survival has been demonstrated to date. This unsatisfactory clinical outlook has sustained the search for alternative or complementary therapeutic modalities, among which immunotherapy and BNCT are currently among the most actively investigated.

BNCT for Glioblastoma multiforme: Clinical Evidence and Outcomes

Glioblastoma multiforme is characterized by an aggressive infiltrative growth pattern that renders complete surgical resection virtually impossible, and by an intrinsic resistance to conventional photon radiotherapy partly attributable to the presence of hypoxic tumor regions [34]. These features have long motivated the investigation of BNCT as an alternative or complementary treatment strategy, given that its cytotoxic mechanism is independent of intracellular oxygen content [34]. Clinical trials of BNCT for GBM have been conducted since the Nineties, initially using reactor-based neutron sources and subsequently with accelerator-based systems. However, a direct comparison of outcomes across studies remains challenging due to the considerable heterogeneity in treatment protocols, boron delivery agents, neutron beam characteristics, and patient selection criteria, as well as the consistently small sample sizes involved [35].

Among the earliest trials, Chadha et al. [36] reported the outcomes of GBM patients treated with BNCT at Brookhaven National Laboratory in the mid-1990s, following surgical resection and administration of BPA-fructose at 250 mg/kg. The median survival of 13 months represented a modest but notable improvement over the historical control of 9.7 months for this tumor type at the time. In Japan, Miyatake et al. [37] described a large cohort of 167 patients with high-grade brain tumors treated between 2002 and 2014, using BPA administered at 200 mg/kg/h prior to and 100 mg/kg/h during neutron irradiation. Median survival for recurrent GBM was 10.8 months, while newly diagnosed patients treated with BNCT alone achieved 15.6 months, rising to 23.5 months when BNCT was combined with adjuvant X-ray radiotherapy [37]. These findings are consistent with the general observation that combining BNCT with conventional photon irradiation may provide a survival advantage over BNCT alone, likely due to complementary mechanisms of cell killing [35].

Kawabata et al. [38] investigated both intraoperative and external beam BNCT in fifteen patients with malignant gliomas, using BSH (5 g per body weight) and BPA (250 mg/kg) respectively. The median time to progression was comparable between the two approaches (approximately 12 months) and the 2-year overall survival reached 53.3%, a figure considerably higher than that typically reported with standard temozolomide-based chemoradiotherapy [38]. In Sweden, a cohort of 30 GBM patients treated with a high-dose f-BPA regimen (900 mg/kg) yielded a median OS of 14.2 months. Kageji et al. [39] reported a median survival of 19.5 months in 23 newly diagnosed GBM patients treated with BSH-based BNCT without chemotherapy, with 2-year and 5-year survival rates of 31.8% and 9.1% respectively, and five patients surviving beyond three years, suggesting that BNCT may confer durable disease control in a subset of patients. In a broader series, Hatanaka and Nakagawa [40] reported 9 long-term survivors exceeding 10 years among 120 patients treated with BNCT, a finding that, while exceptional, highlights the potential of this modality to produce prolonged responses in selected cases.

The observation that combined protocols consistently outperform BNCT alone led to the design of more sophisticated treatment strategies. Yamamoto et al. [41] demonstrated that the addition of external beam radiotherapy to BNCT in newly diagnosed GBM improved median survival from 15.6 months (BNCT alone) to 23.5 months (combined protocol), prompting the initiation of a formal phase II study (OSAKA-TRIBRAIN0902, NCT00974987). The Tsukuba BNCT trial [42] further explored the combination of BPA-based BNCT (250 mg/kg) with X-ray irradiation and adjuvant temozolomide, aligning with the standard Stupp protocol while adding the selective high-LET component of BNCT. Preliminary results from this study reported a median overall survival of 21.1 months and a 2-year OS of 45.5%, figures that compare favourably with the historical benchmark of approximately 14.6 months established by the EORTC-NCIC trial for standard chemoradiotherapy [35].

The transition to accelerator-based BNCT has opened new possibilities for multicenter clinical research. Kawabata et al. [43] published in 2021 the results of the first phase II trial employing a cyclotron-based neutron source (BNCT-30) with a lithium target in Japan. The boron carrier was SPM-011, a ^{10}B-enriched BPA analogue approved as a pharmaceutical agent in Japan, administered at 200 mg/kg/h before and 100 mg/kg/h during irradiation. Among 27 patients with recurrent high-grade gliomas, 24 GBM and 3 WHO grade III, all previously treated with temozolomide and conventional radiotherapy, the 1-year survival rate was 79.2%, decreasing to 54.2% at 18 months and 33.3% at 2 years, results that are particularly encouraging given the refractory nature of the patient population [43]. Consistent with the broader landscape of BNCT clinical research reviewed by Karihtala [35] and Shen et al. [34], these findings suggest that accelerator-based BNCT holds genuine promise for GBM and that the growing availability of hospital-based neutron sources will facilitate the larger, randomized trials necessary to establish BNCT as a standard treatment option within the neuro-oncology armamentarium.

1.5.4 BNCT for Head and Neck Cancer

Head and neck cancer (HNC) is a heterogeneous group of malignancies arising from the mucosal surfaces of the oral cavity, oropharynx, hypopharynx, larynx and nasal and paranasal sinuses. According to global cancer statistics, HNC represents the seventh most prevalent malignancy worldwide, with more than 660000 new diagnoses and approximately 325000 deaths reported annually [34]. Squamous cell carcinoma (SCC) accounts for nearly 90% of all HNC cases, with the remaining fraction comprising a variety of histological subtypes including adenoid cystic carcinoma, mucoepidermoid carcinoma, salivary duct carcinoma and acinic cell carcinoma [44, 45]. The standard of care for early-stage HNC is surgical resection, while locally advanced disease is typically managed with a combination of radiotherapy and platinum-based chemotherapy, achieving a 3-year overall survival rate of approximately 78% [46]. However, despite the availability of multimodal treatment strategies, between 50% and 60% of patients experience locoregional recurrence or distant metastasis within two years of completing primary treatment [34]. The management of locally recurrent HNC (LRHNC) represents one of the most challenging scenarios in oncology: re-irradiation with photon beams is often limited by the tolerance of previously irradiated normal tissues, salvage surgery is frequently not feasible due to anatomical constraints or patient comorbidities, and systemic therapies including immune checkpoint inhibitors yield objective response rates below 20% in the recurrent setting [34]. In the absence of effective treatment options, the median survival of untreated patients with locally recurrent disease is only 6-9 months [34].

In this challenging clinical context, BNCT offers several theoretical and practical advantages that make it a particularly attractive option for HNC. From an anatomical standpoint, head and neck tumors are typically superficially located and accessible to epithermal neutron beams, allowing the delivery of curative doses to the target volume [44]. From a radiobiological perspective, the high-LET radiation generated by the $^{10}B(n,\alpha)^{7}Li$ reaction is effective regardless of the oxygen content of tumor cells, making BNCT potentially active against hypoxic tumor regions that are inherently resistant to conventional photon radiotherapy [34]. Furthermore, the cell-level selectivity of BNCT, enabled by the preferential uptake of boron-containing compounds such as 4-borono-L-phenylalanine (BPA) via the L-type amino acid transporter 1 (LAT1), which is overexpressed in many HNC subtypes, allows for the selective destruction of tumor cells while largely sparing the surrounding normal tissues [45]. This selective mechanism is particularly relevant in the head and neck region, where critical structures including the spinal cord, optic nerves, salivary glands and major vessels lie in close proximity to the tumor, severely constraining the deliverable dose in conventional re-irradiation scenarios.

BNCT for Head and Neck Cancer: Clinical Evidence and Outcomes

Clinical experience with BNCT for recurrent HNC began in Japan in 2001 and was subsequently extended to Finland and Taiwan [45]. Early reactor-based phase I/II trials reported encouraging objective response rates (ORR) consistently exceeding 70% in heavily pre-treated patient cohorts [47, 44, 8, 48]. In a landmark Finnish phase I/II trial enrolling 30 patients with locally recurrent HNC who had previously received photon radiotherapy, Kankaanranta et al. reported a complete response rate of 45%, a 2-year progression-free survival of 20%, and a 2-year overall survival of 30%, with acceptable acute toxicity [8]. A subsequent analysis on 79 patients with inoperable recurrent head and neck SCC further confirmed that fractionated BNCT achieved superior complete response rates compared to single-fraction treatment (50% vs. 19%) [34]. In a Taiwanese phase I/II trial at the Tsing Hua Open-Pool Reactor, Wang et al. demonstrated that fractionated BNCT with adaptive re-planning based on updated tumour-to-normal tissue (T/N) ratios was feasible and safe, reporting an overall response rate of 58% with no grade 4 toxicity [48]. At the University of Tsukuba, Aihara et al. treated 20 patients with advanced or recurrent HNC and reported an effective rate (CR + PR) of 90%, with no severe acute or chronic normal-tissue reactions [44].

The transition from reactor-based to accelerator-based BNCT (AB-BNCT) represented a pivotal advancement for the clinical applicability of this treatment. The JHN002 phase II study, employing a cyclotron-based epithermal neutron source and borofalan (^{10}B) as the boron carrier, demonstrated an ORR of 71% in 21 patients with recurrent or locally advanced HNC, with a 2-year overall survival of 85.3% and a notably low rate of severe adverse events [45, 34]. On the basis of these results, accelerator-based BNCT received regulatory approval in Japan in June 2020, becoming the first BNCT modality covered by the national health insurance system [45]. Real-world data collected at the Kansai BNCT Medical Center over the subsequent two years confirmed the findings of the pivotal trial, with an ORR of 80.5% and 1-year overall survival of 75.4% in 69 patients [45]. A subsequent retrospective study on the initial 47 patients treated under the Japanese national health insurance system reported a complete response rate of 51% and an overall response rate of 74% [34].

The first meta-analysis specifically evaluating BNCT for locally recurrent HNC (LRHNC), published in 2026 by Sun et al., pooled data from seven studies encompassing 361 patients and reported a pooled ORR of 70% (95% CI: 65%–75%) with negligible heterogeneity ($I^2 = 0\%$) and a 2-year overall survival of 45% [46]. Subgroup analyses highlighted a significant dose–response relationship, with patients receiving a minimum tumour dose (D_{min}) exceeding 20 Gy-Eq achieving markedly higher ORR (80% vs. 54%) and 2-year OS (66% vs. 12%) compared to those receiving lower doses [46]. The toxicity profile of BNCT for HNC has generally been considered manageable. The most frequent acute adverse events include hyperamylasemia, alopecia and oral mucositis, while late toxicities encompass alopecia, fatigue and, less commonly, cranial neuropathy and osteonecrosis of the jaw [46]. The most clinically significant severe adverse event remains carotid blowout syndrome, reported in approximately 5% of cases, which requires careful pre-treatment vascular assessment [46, 45].

Summarizing, Glioblastoma multiforme and recurrent or locally advanced head and neck cancers are the main targets of BNCT clinical trials currently active. As explained above, the in vivo radiobiological investigation still plays a pivotal role to better understand and describe the dose-response relation in BNCT, and the results have the potential to improve the quality of the treatment for BNCT patients in the current era of accelerator-based BNCT.

This thesis explores the set-up of the radiobiological experiments in mice at the BNCT facility in Finland and evaluates the possibility to adopt the same solutions at the ANTHEM BNCT centre under construction in Caserta. To this end, a thorough investigation of the dosimetric strategy was carried out, to enable a precise calculation of the absorbed dose in the small volumes of mice organs and tumor. This thesis will also show the capability of the treatment Planning System IT_STARTS developed in Pavia in enabling a complete treatment planning for small animals.

Chapter 2

Preliminary studies and design of a mice holder

The neutron beams available at accelerator-based BNCT facilities are optimized for the treatment of deep-seated tumors in human patients, and therefore deliver epithermal neutrons with energy peaked between 1 and 10 keV. At these energies, neutrons are capable of penetrating some centimeters of tissue before thermalizing, which is precisely the property required to reach deeply located lesions such as glioblastomas in the human brain. However, when the same beam is directed at a small animal such as a mouse, the situation changes substantially: the tumors under investigation are either subcutaneous or shallow, and the overall dimensions of the animal are several orders of magnitude smaller than those of a human patient. Thus, also internal tumors require a penetration depth substantially lower. As a consequence, epithermal neutrons would traverse the entire body of the mouse without undergoing sufficient moderation, depositing dose with poor selectivity, without maximizing the probability of boron capture in the tumor site, compromising both the safety of the animal and the robustness of the radiobiological evaluation.

This thesis was motivated by the need to set-up an in-vivo radiobiological investigation at the BNCT facility in Finland, where I spent some months working in the simulations for the preliminary steps, necessary before starting the real animal irradiation.

The most important preliminary step to enable the radiobiological activity was the design of a dedicated holder for the animals, capable of adapting the beam to the constraints of small-animal irradiation while satisfying a set of physical, biological and regulatory requirements that are discussed in detail in the next section. The holder design had to account simultaneously for the spectral tailoring of the neutron field, the geometrical arrangement of the animals, the animal welfare regulations and the sterility requirements, leading to a configuration whose material composition and geometry were carefully optimized.

After the optimization of the holder, the second step was to evaluate whether charged particle equilibrium (CPE) conditions held in the relevant volumes, to explore the possibility to make dose calculation through KERMA approximation. The major concern was for the photon dose component, which could be significantly far from equilibrium given the small dimensions of the target volumes. This was important because, for the calculation of dose in the mice, we intended to employ the same dosimetric strategy used for human patients (see next Chapter). If CPE is not granted, the relationship between absorbed dose and KERMA is not straightforward and consequently the reliability of the dosimetric approach adopted for treatment planning may not be correct. The goal of this assessment was to understand the discrepancy between dose and KERMA, understanding the amount of overestimation of the dose using CPE approximation.

All simulations and calculations described in the following sections were performed using the Monte Carlo code MCNP6.2 [27], which was employed to transport radiation and to calculate the dose components within the modeled configuration.

A simplified geometrical model of the mouse was constructed to this end. Initial investigations were performed using a basic representation in which the animal was approximated as a homogeneous cylinder. Following these preliminary tests, the model was refined to a slightly more complex yet still idealized geometry, providing a better compromise between anatomical realism and computational tractability. Within the eight-mouse irradiation configuration allowed by the holder structure, only one animal was replaced by the geometrical model, while the remaining positions and representations of the animals were kept unchanged in order to preserve the overall layout of the experimental setup, as shown in Figure 2.3b.

The neutron source employed in these first simulations was modeled with with simplified spectral and spatial characteristics, only representative of BNCT situation.

2.1 Mice holder set-up

The first issue to consider in the design of the holder was how to position the mice: searching for different analog experiments worldwide, it was clear that not all the solution implemented elsewhere were feasible, because several legal constraints had to be taken into account for the national regulation. Finnish and European laws underline the importance of animal wellness and, despite many papers in literature report experiments with mice located radially with the head exposed to the beam port, for Finnish regulation it was forbidden to put the mice upside-down. Interestingly, recent studies suggest that body positioning may influence physiological and metabolic responses to irradiation. In particular, variations in posture can affect blood distribution, tissue oxygenation and stress-related hormonal responses, potentially modulating radiation-induced metabolic effects. Therefore, in compliance with animal welfare regulations that discourage prolonged inverted positioning and to avoid introducing systematic bias in the experimental outcomes, a different solution was pursued. In fact, avoiding potentially stressful handling conditions may reduce confounding stress-related variables, thereby improving the reliability and translational relevance of the metabolic response data. Another important aspect that had to be considered was the risk of an outside contamination: the mice are kept in specific facilities with a sterile environment, so to be transported in hospital to be irradiated, they must be carried in a sealed container, keeping the environment inside the holder as clean as possible to avoid external contamination. To study the two relevant tumors for clinical BNCT (glioblastoma and head and neck recurrent and locally advanced cancers) the body part that needed to be exposed was the head and neck district.

The optimal configuration consisted of eight mice positioned head-to-head as illustrated in the Figure 2.1. While sample size estimations in similar studies often suggest approximately ten animals to ensure adequate statistics, the present design with eight mice was considered sufficient to achieve meaningful results, taking into account both experimental feasibility and ethical considerations as explained above.

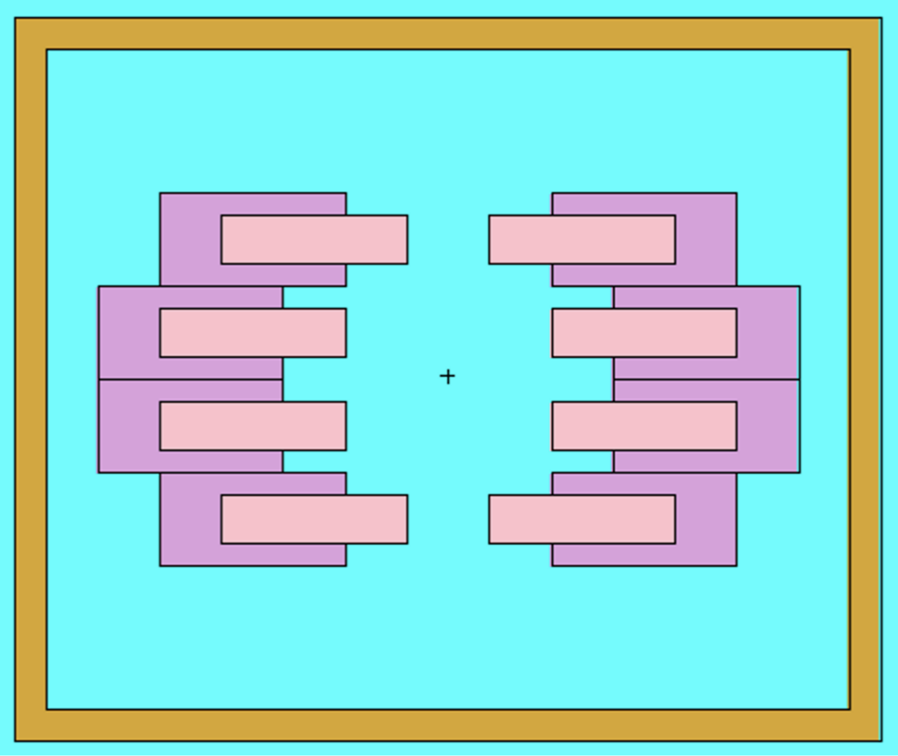

Figure 2.1: MCNP geometry view of the mice arrangement. The incoming beam is perpendicular to the image plane (out-of-plane direction). The PMMA wall is shown in brown, the ^{6}Li-enriched plastic shielding in purple, the mice in pink, and the surrounding air in light blue.

The second important point was the materials and the geometry of the holder to obtain a thermal neutron beam in the relevant parts of the animals. The material that was used for the outside container is PMMA (Polymethyl Methacrylate) that is a transparent and rigid thermoplastic polymer largely used in the medical field. It is considered one of the best candidates to moderate the neutrons until reaching the energy range that are useful for the experiment, being a hydrogenated materials thus allowing an energy shift from epithermal to thermal in few neutrons scattering events. In the Figure 2.1 the PMMA is the external wall represented in brown.

Importantly, the rest of the mice body must be shielded as much as possible not to overcome the tolerance dose in any of the healthy organs. For the mice shielding, represented in the Figure 2.1 as purple rectangles, ^6Li-enriched plastic was used. This material has a high absorption cross section in the thermal neutron energy range, with the additional advantage of not emitting photons in the neutron capture, and so it is useful to stop as much as possible the neutrons reaching the healthy organs, sparing the bodies of the animals outside the target. The dimensions of the holder are shown in the Tables 2.1, 2.2 and 2.3 and they were chosen to take into account the dimension of the collimator of the neutron beam and the optimization of the neutron spectrum. Figure 2.2 shows the actual holder manufactured in Helsinki according to the optimized design. Since the largest neutron collimator available at the Finnish facility has a diameter of 20 cm, the holder was scaled to match this width. The wall thicknesses were optimized to shape the neutron spectrum appropriately: the front wall was set to 2 cm, while the back wall was made substantially thicker at 4 cm, as shown in the Table 2.3, in order to increase the thermal neutron flux at greater depths within the mouse, ensuring adequate dose delivery to the target volume.

Axis	Dimension (cm)
X	15.5
Y	35
Z	42

Table 2.1: External dimensions

Axis	Dimension (cm)
X	9.5
Y	32
Z	39

Table 2.2: Internal air cavity

Walls	Dimension (cm)
Front (beam-facing)	2
Back	4
Lateral	1.5 each

Table 2.3: PMMA walls thicknesses

Inner radius (cm)	Height (cm)
1.5	6

Table 2.4: Mice cylindrical container

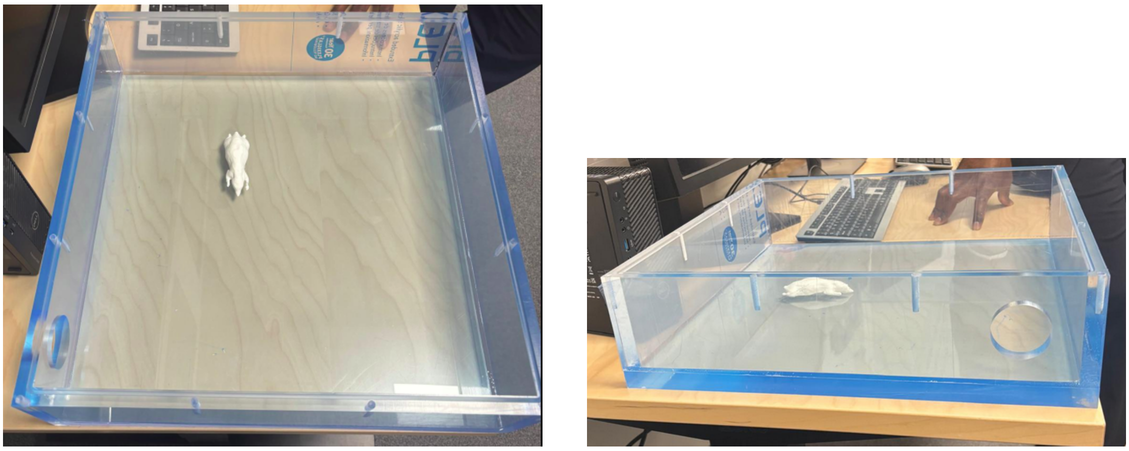

(a) Top view of the holder (b) Side view of the holder

Figure 2.2: The actual holder obtained after this simulation study

2.2 Geometrical Mouse Model

The geometrical mouse model, apart for the cylinder initially used to study the optimization of the holder, is shown in the left panel of Figure 2.3a. The model is intentionally simplified in order to allow controlled dosimetric investigations while preserving the essential anatomical features relevant for BNCT studies.

The geometry consists of the following components:

- A superficial tumor, modeled as a spherical volume (pink sphere in the upper region of Figure 2.3a);
- The brain, represented by an ellipsoidal volume (big light-blue sphere below the pink sphere);
- The heart, modeled as a smaller ellipsoidal volume (light-blue sphere between the 2 orange ellipsoids);
- The lungs, represented by two symmetric ellipsoids (orange volumes);
- The stomach, modeled as a ellipsoidal volume (light-blue ellipsoid under the two orange ellipsoids);
- The bladder, represented by a smaller ellipsoidal volume (light-blue sphere under the bigger light-blue volume);
- The body of the mouse, approximated as a homogeneous cylindrical volume (purple region) with height of 8 cm and radius of 1.5 cm, embedding all internal organs;
- Two lateral ^{6}Li-enriched shielding elements (green regions), included to investigate neutron absorption and shielding effects.

Figure 2.3a, right panel, shows the model in the z–y plane. A sectional view is adopted in order to display simultaneously all the internal structures composing the animal phantom. All organs, including the tumor, are modeled as soft tissue. The elemental composition and density are assumed uniform throughout the body, with the exception of the lungs, for which a reduced density of $0.3\,\mathrm{g\,cm^{-3}}$ is assigned to account for their physiological structure. The boron concentration is assumed homogeneous within each region, with a value of $10\,\mathrm{ppm}$ in all healthy tissues and $50\,\mathrm{ppm}$ in the tumor. This choice reflects the differential boron uptake expected between malignant and normal tissues and allows investigation of the therapeutic gain under controlled conditions.

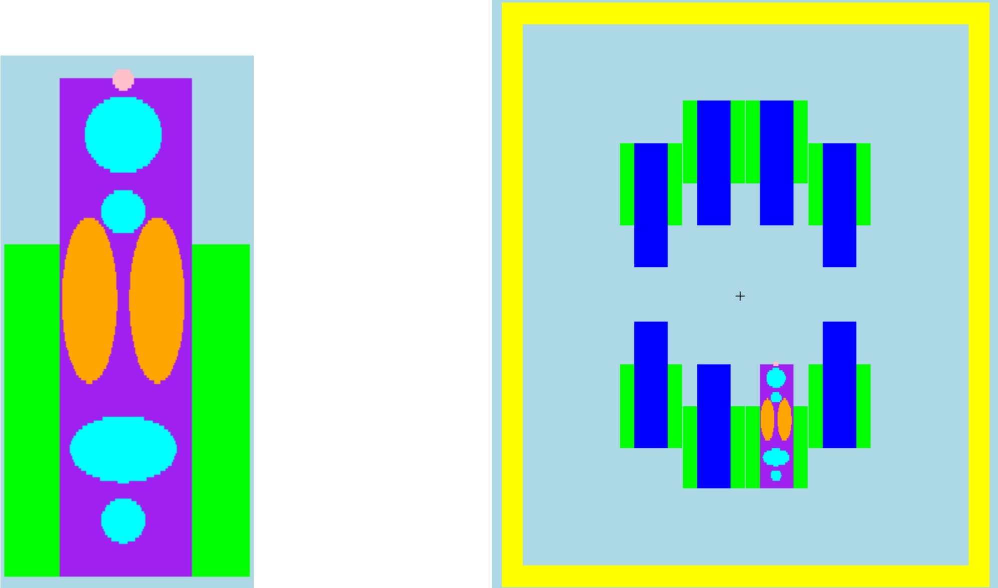

(a) Geometrical mouse model used in the simulations (sectional view in the z–y plane).

(b) FOV of the mice holder with the geometrical model.

Figure 2.3: MCNP representation of the geometrical model (left) and the position in which the geometrical model is located in the mice holder (right).

2.3 Neutron Source

The neutron source adopted in this first set of simulations is shown in Figure 2.4. The beam port is modeled as a truncated conical polyethylene structure with a length of $30\,\mathrm{cm}$, a base diameter of $40\,\mathrm{cm}$, a diameter of $15\,\mathrm{cm}$ and the distance between the holder and the truncated conical source is $1.88\,\mathrm{cm}$. The simplified geometry is designed to reproduce the essential geometrical characteristics of an accelerator-based BNCT beam-shaping assembly while maintaining computational efficiency. Although the distance between the set-up and the beam port should be ideally zero, to avoid loss of neutrons, this distance represents a physical constraint due to the positioning tools used to keep the holder in its position, built at the Finnish facility.

The flight direction of the emitted neutron beam is sampled within a conical angular aperture of $20°$.

The energy spectrum is composed of the following components:

- 10% thermal neutrons ($E < 0.2\,\mathrm{eV}$),
- 80% epithermal neutrons ($0.2\,\mathrm{eV} \leq E \leq 40\,\mathrm{keV}$),
- 10% fast neutrons ($40\,\mathrm{keV} \leq E \leq 0.5\,\mathrm{MeV}$).

This spectral distribution, shown in the Figure 2.5, is chosen to represent an epithermal energy spectrum typically required in BNCT, where epithermal neutrons are responsible for adequate penetration into tissue before thermalization and subsequent capture reactions.

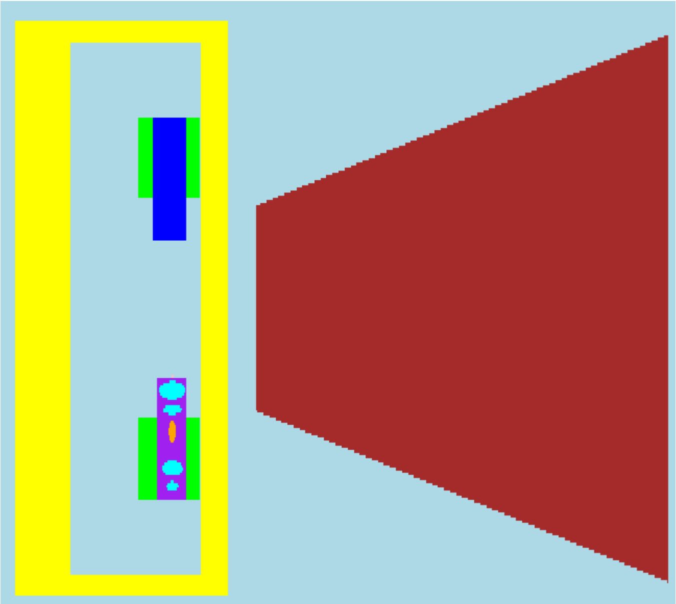

Figure 2.4: z–x plane view of the neutron source and beam configuration.

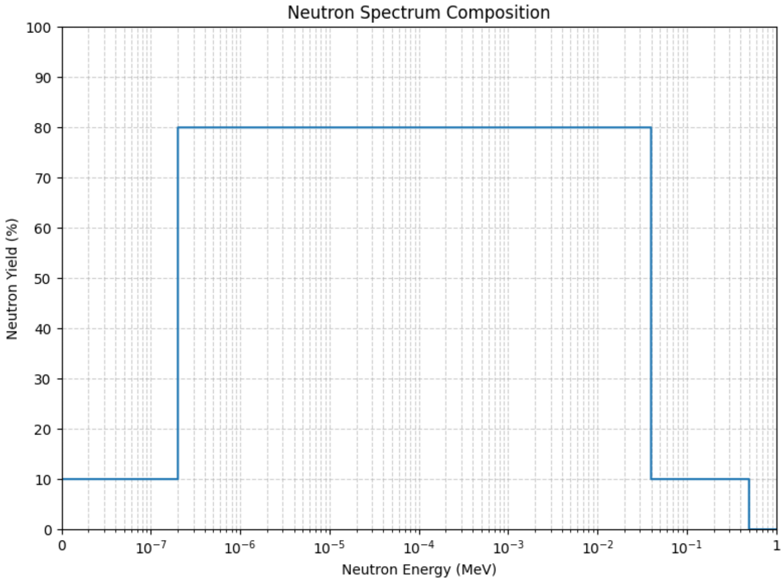

Figure 2.5: Neutron Spectrum used for the equilibrium studies

2.4 Equilibrium Studies

A preliminary and fundamental aspect in BNCT dosimetric investigations is the verification of charged-particle equilibrium conditions. In particular, it is necessary to assess whether the photons generated by neutron capture reactions, mainly the $^1\mathrm{H}(n,\gamma)^2\mathrm{H}$ process, are locally absorbed within the volume of interest. This verification is essential because the equality between absorbed dose and collision KERMA,

$$D = K_c \tag{2.1}$$

is valid only under well–defined physical conditions, as it is described in the 1.5.4.

2.4.1 Condition for $D = K_c$

As described in the Introduction, in a medium irradiated by indirectly ionizing radiation (such as neutrons or photons), the absorbed dose D differs in general from KERMA K, since KERMA represents the kinetic energy transferred to charged secondary particles, whereas dose represents the energy actually deposited locally by those particles.

The relationship

$$D = K_c \tag{2.2}$$

holds when Charged-Particle Equilibrium (CPE) is satisfied and when radiative losses are negligible. More precisely, CPE exists at a point if, for every charged particle of a given type and energy leaving an infinitesimal volume surrounding that point, an identical charged particle enters it. Under these conditions, the net energy carried in and out by secondary charged particles is zero, and therefore the energy transferred to charged particles (collision KERMA) is entirely dissipated locally as absorbed dose.

Formally, the absorbed dose at a point can be written as:

$$D = K_c - \nabla \cdot \vec{J}_E \tag{2.3}$$

where $\vec{J}_E$ is the charged-particle energy flux vector. When CPE holds,

$$\nabla \cdot \vec{J}_E = 0 \tag{2.4}$$

and therefore:

$$D = K_c \tag{2.5}$$

CPE is typically satisfied in regions where:

- The medium is homogeneous in composition and density;
- The radiation field is spatially uniform;
- The point considered is sufficiently far from boundaries and interfaces;
- The range of secondary charged particles is small compared to the dimensions of the region.

Conversely, CPE fails near interfaces, in build-up regions or when strong spatial gradients in particle fluence are present. In such cases, dose and KERMA differ and cannot be used interchangeably.

2.4.2 MCNP Tallies for Equilibrium Assessment

To verify whether the condition $D = K_c$ can be reasonably assumed in the present BNCT configuration, MCNP track-length tallies were employed. In particular, the F4:n tally-type was used to calculate the neutron fluence averaged over a cell and normalized per simulated source particle:

$$\Phi = \frac{\text{neutrons}}{\text{cm}^2 \cdot \text{NPS}} \tag{2.6}$$

where NPS denotes the number of source particles.

In order to convert neutron fluence into absorbed dose contributions corresponding to the different BNCT components, the F4 tally was coupled with the FM multiplier card. The FM card weights the fluence by the appropriate microscopic reaction cross sections from the MCNP nuclear data libraries, allowing the estimation of reaction rates and associated energy deposition. The general form of the multiplier card, as shown in the Figures 2.6 where all the four components of the BNCT are visible, is:

$$\text{FM}n\ C\ M\ R$$

where:

- M is the material number assigned in the geometry definition;
- R identifies the nuclear reaction of interest:
  - $R = 103$ for (n, p) reactions,
  - $R = 107$ for (n, α) reactions,
  - $R = 102$ for (n, γ) reactions,
  - $R = 2$ for elastic scattering,
  - $R = -4$ for energy deposition (heating number).
- C is a normalization constant introduced to convert reaction rate per source particle into absorbed dose expressed in Gy.

The normalization constant is defined as:

$$C = \frac{N \cdot N_A \cdot E}{A} \times (1.6 \times 10^{-19}) \times 10^{-24} \times 10^3\ Gy \tag{2.7}$$

where:

- N is the atomic density of the material,
- A is the atomic weight of the material,
- N_A is Avogadro's number,
- E is the energy released per reaction (in eV),
- 10^{-24} converts barns to cm^2,
- 1.6×10^{-19} converts eV to Joules,
- 10^3 converts grams to kilograms.

Through this procedure, the individual BNCT dose components can be derived from neutron fluence and comparison between collision KERMA and absorbed dose allows verification of the validity of the equilibrium assumption within the modeled geometry.

When the FM multiplier card is employed, it implicitly assumes that the 2.2 MeV photons generated by neutron capture in hydrogen are fully absorbed within the volume of interest. This corresponds to the condition of charged-particle equilibrium (CPE), under which the KERMA can be considered equal to the absorbed dose. In order to verify the validity of this approximation, the FM4 results must be compared with alternative tallies that provide a more explicit evaluation of local energy deposition. Although these tallies are computationally more expensive in terms of simulation time, they offer a more rigorous description of photon–electron transport. For this purpose, the *F8 tally was employed, as shown in Figure 2.7. The *F8:E tally scores the pulse-height distribution associated with electron energy deposition resulting from photon interactions. To obtain the absorbed dose, the tally output must be normalized to the mass of the scoring cell.

The F6:P tally, instead, provides a track-length estimate of the energy deposition for a specified particle type on a cell basis, expressed in units of MeV/g per source particle [27]. Unlike the FM4 tally, which relies on KERMA coefficients, these tallies directly account for the total energy locally deposited by primary particles, relying on internal factors, not available to the user.

It should be noted that the following discussion on radiation equilibrium is restricted to photons. For charged particles, radiation equilibrium is assumed to hold a priori. This assumption is justified by the fact that the characteristic ranges of charged particles (such as protons, alpha particles and recoil nuclei) in the considered materials are significantly smaller than the dimensions of the tumor or, more generally, of the regions of interest in the simulation. As a consequence, their energy can be considered to be locally deposited within the same region in which they are generated, leading to the validity of charged particle equilibrium (CPE).

Under these conditions, the contribution of charged particles to the absorbed dose can be evaluated assuming complete local energy deposition, without the need to explicitly account for their transport across the boundaries of the tumor.

In contrast, photons exhibit much longer mean free paths and can travel distances comparable to or larger than the size of the tumor. Therefore, photon transport may result in a net energy exchange between neighboring regions, and radiation equilibrium cannot be assumed a priori. For this reason, the analysis of radiation equilibrium is explicitly carried out only for the photon component.

2.4.3 Results for Equilibrium Assessment

As reported in Table 2.5, not all the values obtained with the different tallies for the photon component are in good agreement. The FM4 results are systematically higher than the corresponding F6 values, reflecting possible differences in the underlying KERMA factors and cross-sectional data. Moreover, because the calculation allowed the transport of electrons, F6 accounts for possible deposition of dose outside the target and it does not assume total energy deposition in the cell. On the contrary, F4+Fm strategy assumes that all the energy is deposited in the point of interaction. Nevertheless, for the organs located inside the shielding, the condition of charged-particle equilibrium can be reasonably assumed. The maximum percentage difference observed between the F6 tally and the mass-normalized *F8 tally in the organs inside the body is approximately 17%. This result indicates that replacing the computationally intensive *F8 tally with the F6 tally introduces a maximum uncertainty of about 17% in the photon dose component, while significantly reducing simulation time and computational cost. Within the framework of the present equilibrium assessment, this deviation was considered acceptable. It must be recalled that this is only one of four dose contributions, thus a discrepancy of the order of 10% can be neglected. This is also true considering that the highest source of error in dose deposition due to BNCT is the actual value of boron concentration in the tumor of animal models and in all the organs. This is usually assumed equal to typical values but it might be affected by the biological variability. A larger discrepancy between the two quantities was expected for the tumor region, due to its small size and superficial location.

To further clarify the relevance of the photon dose contribution to the total absorbed dose in the tumor, a comparison between the sum of the four dose components and the corresponding four KERMA components was performed. The percentage difference between total dose and total KERMA was evaluated by computing these quantities, all reported in Table 2.6, through two distinct approaches:

- The total absorbed dose was obtained as the sum of the elastic scattering, proton and alpha components, while the photonic contribution was evaluated using the **F8* tally normalized to the cell mass.
- The total KERMA was calculated as the sum of the same three components (elastic scattering, protons and alphas), whereas the photonic component was derived from the *F6* tally.

Once both total dose and total KERMA were determined, the relative percentage difference was calculated according to:

$$\frac{(\text{total KERMA} - \text{total dose})}{\text{total dose}} \times 100. \tag{2.8}$$

The observed difference amounts to approximately 17%. This result highlights the importance of carefully accounting for the photonic component through the use of the *F8/mass tally instead of the F4, since the tumor may receive a lower absorbed dose than that predicted by the Treatment Planning System when KERMA-based estimations are adopted.

It should be noted, however, that in the subsequent Chapter, where the Treatment Planning System is fully applied, the tumor is positioned within the mouse body rather than at a very superficial location as in this model. Under those conditions, a reduced discrepancy between KERMA-based and energy-deposition-based estimations is expected. The tumor was placed in this critical position for the purpose of an initial verification in the worst-case scenario. This configuration represents the most critical limiting case, as it corresponds to the situation in which the dosimetric error introduced by the equilibrium assumption reaches its maximum possible value, estimated, as seen, to be approximately 17%. In case this corresponds to the real mice tumor, the treatment planning can still be carried out with KERMA approximation, taking into account this overestimation due to incorrect assumption of CPE conditions for the photon component.

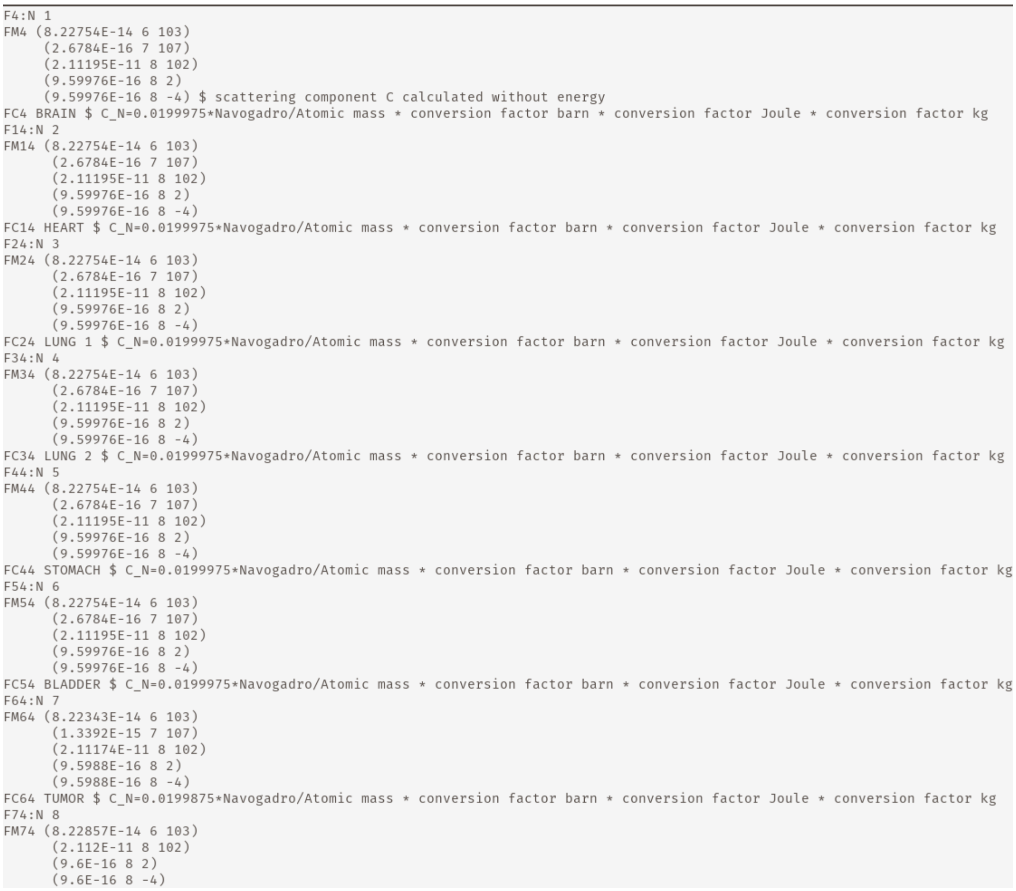

```
F4:N 1
FM4 (8.22754E-14 6 103)
     (2.6784E-16 7 107)
     (2.11195E-11 8 102)
     (9.59976E-16 8 2)
     (9.59976E-16 8 -4) $ scattering component C calculated without energy
FC4 BRAIN $ C_N=0.0199975*Navogadro/Atomic mass * conversion factor barn * conversion factor Joule * conversion factor kg
F14:N 2
FM14 (8.22754E-14 6 103)
      (2.6784E-16 7 107)
      (2.11195E-11 8 102)
      (9.59976E-16 8 2)
      (9.59976E-16 8 -4)
FC14 HEART $ C_N=0.0199975*Navogadro/Atomic mass * conversion factor barn * conversion factor Joule * conversion factor kg
F24:N 3
FM24 (8.22754E-14 6 103)
      (2.6784E-16 7 107)
      (2.11195E-11 8 102)
      (9.59976E-16 8 2)
      (9.59976E-16 8 -4)
FC24 LUNG 1 $ C_N=0.0199975*Navogadro/Atomic mass * conversion factor barn * conversion factor Joule * conversion factor kg
F34:N 4
FM34 (8.22754E-14 6 103)
      (2.6784E-16 7 107)
      (2.11195E-11 8 102)
      (9.59976E-16 8 2)
      (9.59976E-16 8 -4)
FC34 LUNG 2 $ C_N=0.0199975*Navogadro/Atomic mass * conversion factor barn * conversion factor Joule * conversion factor kg
F44:N 5
FM44 (8.22754E-14 6 103)
      (2.6784E-16 7 107)
      (2.11195E-11 8 102)
      (9.59976E-16 8 2)
      (9.59976E-16 8 -4)
FC44 STOMACH $ C_N=0.0199975*Navogadro/Atomic mass * conversion factor barn * conversion factor Joule * conversion factor kg
F54:N 6
FM54 (8.22754E-14 6 103)
      (2.6784E-16 7 107)
      (2.11195E-11 8 102)
      (9.59976E-16 8 2)
      (9.59976E-16 8 -4)
FC54 BLADDER $ C_N=0.0199975*Navogadro/Atomic mass * conversion factor barn * conversion factor Joule * conversion factor kg
F64:N 7
FM64 (8.22343E-14 6 103)
      (1.3392E-15 7 107)
      (2.11174E-11 8 102)
      (9.5988E-16 8 2)
      (9.5988E-16 8 -4)
FC64 TUMOR $ C_N=0.0199875*Navogadro/Atomic mass * conversion factor barn * conversion factor Joule * conversion factor kg
F74:N 8
FM74 (8.22857E-14 6 103)
      (2.112E-11 8 102)
      (9.6E-16 8 2)
      (9.6E-16 8 -4)
```

Figure 2.6: The tallies for the equilibrium condition evaluation, based on F4 tally type.

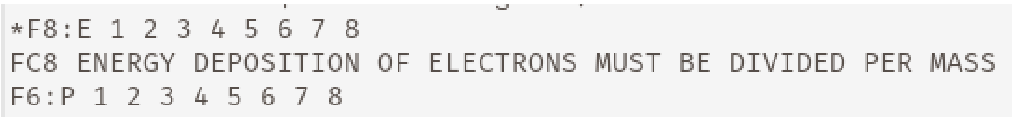

```
*F8:E 1 2 3 4 5 6 7 8
FC8 ENERGY DEPOSITION OF ELECTRONS MUST BE DIVIDED PER MASS
F6:P 1 2 3 4 5 6 7 8
```

Figure 2.7: The tallies for the equilibrium condition evaluation, based on F8* and F6 tally types.

Organs	FM4 [Mev/gr]	*F8/mass [Mev/gr]	F6 [Mev/gr]	$\frac{F6-(*F8/mass)}{*F8/mass} \times 100$
Brain	3.9429×10^{-5}	1.1476×10^{-5}	1.2491×10^{-5}	8.8 %
Heart	2.6439×10^{-5}	1.0418×10^{-5}	1.0823×10^{-5}	3.9 %
Lung 1	7.9733×10^{-6}	7.4325×10^{-6}	8.6989×10^{-6}	17.0 %
Lung 2	7.7345×10^{-6}	7.9572×10^{-6}	8.6515×10^{-6}	8.7 %
Stomach	8.3989×10^{-7}	4.7723×10^{-6}	4.8783×10^{-6}	2.2 %
Bladder	1.5817×10^{-6}	5.2842×10^{-6}	5.2700×10^{-6}	0.3 %
Tumor	4.6540×10^{-5}	6.2731×10^{-6}	1.3352×10^{-5}	112.8 %
Whole Body	8.0933×10^{-6}	4.3775×10^{-6}	5.4502×10^{-6}	24.5 %

Table 2.5: Results of the tally calculations for the all the organs in the simplified animal model.

Dose component	FM4 [Mev/gr]	*F8/mass [Mev/gr]	F6 [Mev/gr]
Photons	4.6540×10^{-5}	6.2731×10^{-6}	1.3352×10^{-5}
Elastic Scattering	2.6513×10^{-7}		
Nitrogen component	9.9734×10^{-7}		
Boron component	3.4152×10^{-5}		

Sum all FM4 + (*F8/mass)	Sum all FM4 + F6	$\frac{(Sum\ FM4+F6)-(Sum\ FM4+(*F8/mass))}{Sum\ FM4+(*F8/mass)} \times 100$
4.1687×10^{-5}	4.8767×10^{-5}	17.0 %

Table 2.6: The four absorbed dose components in the tumor, with the assumption of CPE, the three tally definition and in the table below the total absorbed dose and the total KERMA and the percentage of difference between the two.

2.4.4 Spectra comparison with a more realistic neutron source

A relevant aspect to be investigated is whether the highly simplified neutron source described in the previous section, adopted for the equilibrium assessment, is capable of providing results comparable to those obtained with a more realistic neutron spectrum. To this end, a comparison has been carried out between the simplified spectrum, shown in Figure 2.5, and a more realistic one, reported in Figure 2.8. In the latter case, while a more accurate energy distribution is considered, the additional complexity associated with the angular distribution of the particles is still neglected. In particular, neutrons are assumed to be uniformly distributed within a cone of 20°, using the same spectrum for all the flight directions. This approach enables the isolation of the effect of the energy distribution, allowing for a clearer assessment of its impact on the relevant physical quantities without the influence of angular effects. In this framework, it is possible to evaluate to what extent the simplified model reproduces the main features of a more realistic irradiation scenario, as well as whether it provides sufficiently accurate results for equilibrium-related analyses. Should this assumption be validated, the simplified source can be retained for subsequent analysis, as it significantly reduces the computational cost while preserving an acceptable level of accuracy.

Energy (MeV)	n fluence (simple spectrum) $cm^{-2}/source_n$	n fluence (realistic spectrum) $cm^{-2}/source_n$
5.00×10^{-7}	1.2807×10^{-3}	1.3506×10^{-3}
1.00×10^{-2}	4.0813×10^{-4}	2.8081×10^{-4}
1.00	1.2393×10^{-5}	5.3629×10^{-6}
Total	1.7013×10^{-3}	1.6368×10^{-3}

Table 2.7: Comparison of the neutron fluence per unit of cource neutron in different energy ranges between the simplified and realistic neutron spectra in the tumor.

As shown in Table 2.7, the thermal component of the neutron flux in the tumor is essentially unchanged between the two cases. Consequently, the dose delivered to the tumor is expected to be very similar, since in BNCT the tumor dose is primarily driven by the boron contribution, which depends predominantly on the thermal neutron flux. The induced photon component is also

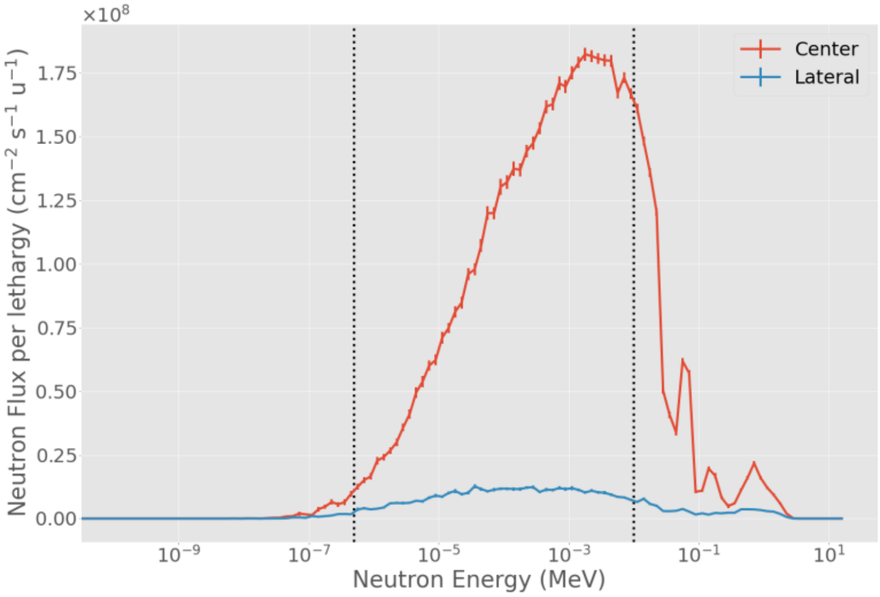

Figure 2.8: BSA energy spectra at the surface of the beam-port. Red line: energy spectrum in a 6 cm radius disk, corresponding to the beam-port. Blue line: spectrum in a ring with minimum radius of 6 cm and maximum radius of 12 cm. The two vertical dotted lines separate the thermal-to-epithermal (0.5 eV) and epithermal-to-fast (10 keV) energy ranges. Illustration from [12]

expected to be the same, as it again depends on capture. On the other hand, the slightly lower epithermal and fast components observed in the realistic spectrum suggest a possible reduction in the dose contribution associated with scattering processes, potentially leading to minor variations in the required irradiation time (see next chapter for more details about the calculation of the treatment time).

The percentage difference between the total KERMA and the total absorbed dose, calculated as described in the previous section, was found to be 16.6%, as shown in Table 2.8. This result is very similar to the obtained with the simplified source and so, also in this case, it is important to carefully account for the photonic component through the use of the *F8/mass tally instead of the F6.

Sum all FM4 + (*F8/mass)	Sum all FM4 + F6	$\frac{(Sum\ FM4{+}F6)-(Sum\ FM4{+}(*F8/mass))}{Sum\ FM4{+}(*F8/mass)} \times 100$
4.4397×10^{-5}	5.1789×10^{-5}	16.6 %

Table 2.8: The total absorbed dose, the total KERMA and the percentage of difference between the two.

Overall, the transition from a highly simplified spectrum, characterized by a coarse and nearly flat representation of the epithermal region (Figure 2.5), to a more realistic spectral distribution (Figure 2.8) with many energy bins, does not produce significant variations in the results. Therefore, for preliminary analyses, the use of a simplified neutron source can be considered justified.

Nevertheless, simulations with the ANTHEM neutron beam have also been performed in order to assess the impact of a fully real description, including both spectral and angular characteristics of the neutron field.

The corresponding results are presented in the following section.

2.4.5 Spectra comparison and Dose-KERMA evaluation with the neutron source ANTHEM

The previously considered sources are idealized not only in terms of their energy distribution, concerning the simplified source, but also with respect to their angular characteristics, as neutrons are assumed to be uniformly distributed within a 20° cone. In contrast, a real beam such as ANTHEM exhibits a more complex angular structure, with a double differential spectrum. In addition, the presence of prompt gamma contamination originating from the primary beam must be taken into account. Although the Beam Shaping Assembly (BSA) is specifically designed to suppress this component, it cannot be completely eliminated. This raises the question of whether the photon contribution may significantly affect the total weighted dose, especially in the case of superficial tumors, as considered in this work. Under these conditions, the validity of the KERMA-dose approximation could, in principle, be compromised, since it relies on the assumption of charged particle equilibrium, which may not be fully satisfied near the surface in the presence of a non-negligible photon component.

The simulation setup follows the configuration described in the previous section: the irradiation holder is identical to that shown in Figure 2.3b, positioned at the same distance and the murine model corresponds to the geometrical phantom illustrated in Figure 2.3a. The only modification concerns the neutron source: instead of the simplified source adopted in the preceding sections, the present analysis makes use of the entire ANTHEM source, described in the Introduction. For this source, the spectrum is equal to the one shown in Figure 2.8 only in the forward direction.

Energy (MeV)	n fluence (simple spectrum) $cm^{-2}/source_n$	n fluence (realistic spectrum) $cm^{-2}/source_n$	n fluence (ANTHEM beam) $cm^{-2}/source_n$
5.00×10^{-7}	1.2807×10^{-3}	1.3506×10^{-3}	2.3352×10^{-6}
1.00×10^{-2}	4.0813×10^{-4}	2.8081×10^{-4}	2.9840×10^{-6}
1.00	1.2393×10^{-5}	5.3629×10^{-6}	2.2845×10^{-7}
Total	1.7013×10^{-3}	1.6368×10^{-3}	5.5477×10^{-6}

Table 2.9: Comparison of the neutron fluence values per unit of source neutron at different energy ranges among simplified, realistic and ANTHEM neutron beams in the tumor.

From Table 2.9, it can be observed that, when using the real ANTHEM beam, the calculated flux is order of magnitude lower than in the ideal cases. However, this is the flux calculated per unit of source neutron and the normalization of the two types of sources (n/sec) are completely different. In the simplified source model, neutrons are assumed to originate directly at the beam port and are subsequently transported through the geometry. The tallies are therefore normalized per source neutron emerging from the beam port. In contrast, in the ANTHEM configuration, the source of neutrons was generated upstream and traverse part of the BSA, including collimation and shielding components. As a consequence, a substantial fraction of particles is lost within the beam shaping assembly, leading to a reduced number of neutrons reaching the scoring region per initial source particle. For this reason, the absolute values of the flux are not directly comparable between the two source models, since they do not share the same reference origin. The observed differences are therefore dominated by normalization and transport losses rather than by intrinsic spectral effects.

A meaningful comparison can instead be performed in terms of relative quantities, such as the thermalization fraction, which is reported in Table 2.10.

Beam	$(Thermal\ component/Total) \times 100$
Simplified	75%
Realistic	82%
ANTHEM	42%

Table 2.10: Percentage of thermal component in the total spectrum for the different spectra.

In this case, the ANTHEM beam produces a lower thermal component in the tumor (42%), compared to the ideal beams. This might have two effects: the production of a lower quantity of radiative gamma rays from hydrogen capture, but also a lower predominance of boron dose over the total dose. On the other hand, the photon contribution may differ significantly due to the presence of primary beam gamma contamination. Thus, the analysis to quantify the impact of these effects on the validity of the KERMA–dose approximation was carried out.

The MCNP tallies employed for the equilibrium assessment are the same as described above.

Organs	FM4 [Mev/gr]	*F8/mass [Mev/gr]	F6 [Mev/gr]	$\frac{F6-(*F8/mass)}{*F8/mass} \times 100$
Brain	7.7596×10^{-8}	2.2638×10^{-8}	2.6117×10^{-8}	15.4 %
Heart	5.5942×10^{-8}	2.2701×10^{-8}	2.4750×10^{-8}	9.0 %
Lung 1	1.9069×10^{-8}	1.9825×10^{-8}	2.3779×10^{-8}	19.9 %
Lung 2	1.8039×10^{-8}	1.9765×10^{-8}	2.2307×10^{-8}	12.9 %
Stomach	3.2211×10^{-9}	1.5741×10^{-8}	1.6901×10^{-8}	7.4 %
Bladder	4.7467×10^{-9}	1.9281×10^{-8}	2.0620×10^{-8}	6.9 %
Tumor	8.3008×10^{-8}	1.4797×10^{-8}	2.2198×10^{-8}	50.0 %
Whole Body	1.6701×10^{-8}	1.1954×10^{-8}	1.5148×10^{-8}	26.7 %

Table 2.11: Results of the tally calculations for the all the organs in the simplified animal model with ANTHEM neutron source.

Despite the effects described above that could impair the conclusions drawn in the ideal cases, no significant impact on the validity of the KERMA-dose approximation is observed. Although the presence of a photon component could, in principle, affect the dosimetric balance, its contribution is only slightly more relevant, due to the effective suppression provided by the BSA. In particular, the maximum observed discrepancy between KERMA and dose for the photon component amounts to approximately 19.9% (Table 2.11). While this value is not negligible, it remains within an acceptable range provided that it is understood and considered when the radiobiological evaluations are carried out after the experiments.

Again, the difference in orders of magnitude observed between the results of the tally calculated per unit of source neutron reported in Tables 2.5 and 2.11 is primarily a consequence of the different normalization of the neutron sources, as discussed in the previous section. However the % difference between kerma and dose can be used as a benchmark. Also in this case, the fraction of thermal neutrons with respect to the total spectrum, shown in Table 2.10 is a meaningful insight, allowing for a physical interpretation of the results, independent of source normalization.

The impact of the thermalization level observed with the ANTHEM beam will be further investigated in the following chapter dedicated to Treatment Planning.

Overall, the analysis highlights that a real neutron field is characterized by both a non-trivial angular distribution and a residual photon contamination originating from the primary beam. However, under the conditions considered in this study, the photon contribution to the discrepancy between dose and KERMA is not dramatically different.

Finally, it is worth noting that the thermal neutron fraction plays a key role not only in determining the boron dose contribution, but also in influencing photon production, since neutron capture reactions in hydrogen are more likely at thermal energies. A reduction in the thermal component may therefore partially compensate for the photon contribution originating from the source itself. Although this effect is not dominant, it suggests a non-trivial interplay between neutron thermalization and photon production, which may deserve further investigation.

Chapter 3

Treatment Planning for BNCT of small animals

3.1 IT_STARTS: Treatment Planning System

The Innovative Toolkit to Simulate neuTron cApture theRapy irradiaTion and doSimetry (IT_STARTS) is a computational Treatment Planning System (TPS) specifically developed for Boron Neutron Capture Therapy (BNCT). The project originates from a collaboration between the BNCT research group of Pavia and the Treatment Planning and Computational Dosimetry group at the Comisión Nacional de Energía Atómica (CNEA, Buenos Aires). The primary objective of IT_STARTS is to provide a flexible, research-oriented platform capable of integrating Monte Carlo radiation transport simulations with advanced radiobiological modeling for BNCT treatment planning [49].
IT_STARTS is written in Python, an open-source programming language chosen for its versatility, modularity and wide scientific adoption. Following a formal validation process, the software is intended to be distributed through appropriate sharing mechanisms in order to facilitate its use within the international BNCT community.

The system is conceived as a modular environment composed of two main components: a geometry and physical dose calculation module and a radiobiological dose processing module, interconnected through external Monte Carlo particle transport codes. The first module is dedicated to patient geometry reconstruction and physical dose evaluation. It allows the transformation of medical imaging data, provided in standard formats such as DICOM or NIFTI, into a voxelized computational model suitable for radiation transport simulation. The corresponding segmentation files (RTSTRUCT) are processed to define the Gross Tumor Volume (GTV) and the Organs at Risk (OARs), generating masks that enable region-specific dosimetric analysis. The resulting voxelized geometry is automatically exported in the input syntax of widely used Monte Carlo transport codes, including MCNP6, PHITS and GEANT4. In this way, IT_STARTS acts as an interface between clinical imaging data and high-precision particle transport simulations. The Monte Carlo simulation stage reproduces the neutron beam configuration and models the full radiation transport within the patient geometry. A scoring mesh can be superimposed on the voxelized model to obtain a detailed voxel-by-voxel evaluation of the absorbed dose rate. In the context of BNCT, the absorbed dose is decomposed into its four physical components: boron dose, proton dose, neutron dose and photon dose. The toolkit enables the systematic calculation and spatial analysis of each component, thus providing a comprehensive physical characterization of the treatment scenario.

The second module of IT_STARTS constitutes the dose engine, which converts the physical absorbed dose components into photon-equivalent dose. This process can be performed using either the conventional RBE-weighted approach or the more advanced Photon Isoeffective Dose model. A distinctive feature of the system is the possibility of importing radiobiological survival data and performing dose–response curve fitting in order to extract the parameters required for radiobiological modeling. This capability allows a coherent integration of experimental radiobiological information into the treatment planning workflow. Beyond physical and photon-equivalent dose distributions, IT_STARTS provides clinically relevant radiobiological indicators, such as Tumor Control Probability (TCP) and Normal Tissue Complication Probability (NTCP), when the radiobiological and dosimetric models are available. The inclusion of these figures of merit enables a quantitative evaluation of both therapeutic efficacy and normal tissue safety, contributing to an informed assessment of the treatment plan [50].

As in conventional clinical TPSs, the software generates isodose curves and Dose–Volume Histograms (DVHs) for target volumes and OARs. However, unlike standard clinical planning systems, IT_STARTS is designed with strong flexibility for research applications. It allows detailed inspection of individual BNCT dose components, comparison between different radiobiological models, and evaluation of alternative beam configurations. For this reason, the system represents a valuable tool not only for pre-clinical and clinical planning studies, but also for methodological investigations aimed at improving BNCT dosimetry and radiobiological modeling. Recently, the possibility to couple IT_STARTS with AI methods to allow for automatic tumor contouring as been proved successfully [50].

In summary, IT_STARTS provides an integrated computational framework that links patient-specific geometry reconstruction, Monte Carlo radiation transport and advanced radiobiological dose evaluation. Its modular design, multi-code compatibility and implementation of innovative dose formalisms make it a powerful and versatile instrument for both clinical-oriented research and dosimetric studies in BNCT. The work described in the following pages shows another use of the TPS, i.e., the treatment planning for small animal models, a feature that the TPS used in clinical BNCT (adapted from standard TPS with the addition of a dose engine for neutron irradiation) do not have.

3.2 Voxelized Mouse Model

Thanks to the first module of IT_STARTS, a voxelized model of a true mouse was generated using a micro-CT scan of an animal model. The detailed model of the mouse substituted one of the cylindrical models into the simulated holder. The simulation of the voxelized model is shown in Figure 3.1. The voxel dimensions are $4.02 \times 3.03 \times 7.95\ mm^3$. This is a generic murine model, however by adjusting the dimensions of the animal model it is possible to perform imaging of any animal model, depending on the radiobiological experiment being conducted.

The use of a detailed voxel-based murine model derived from micro-CT imaging offers several advantages over simplified analytical geometries in Monte Carlo simulations for BNCT treatment planning:

- Dosimetric accuracy: a detailed model faithfully reproduces the real geometry of the organs, reducing uncertainties in dose estimation. Small organs such as salivary glands or olfactory bulbs, which are often neglected or approximated in simplified models, may receive significant doses that would otherwise be underestimated. The proximity to what is carried out for patients make this treatment planning more robust and help the transferability of results.
- Tissue heterogeneity: a voxelized model captures variations in density and composition between tissues, which directly affect neutron transport and local dose deposition.
- Anatomical realism. The shape and position of organs varies from animal to animal. A model derived from real imaging eliminates the simplified geometric assumptions (such as spheres, ellipsoids or cylinders) typical of analytical phantom models.
- Identification of unexpected critical organs. With a simplified model, there is a risk of overlooking organs that, due to their real anatomical position, are located in high-dose regions. A detailed model reveals them automatically.

Overall, the possibility to obtain detailed dosimetry with great precision, allows to produce robust radiobiological data that can be used to inform models for photon isoeffective dose in patients, which is the ultimate goal for an effective clinical BNCT.

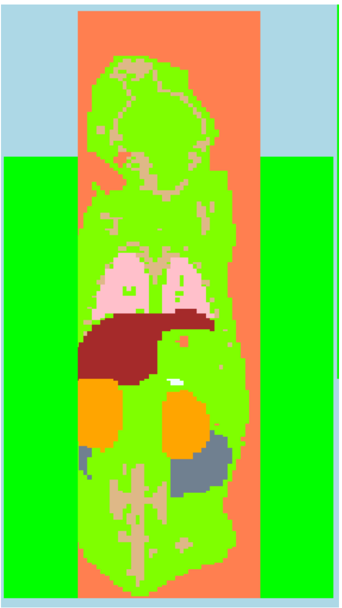

Figure 3.1: Voxelized mouse model used in the simulations (sectional view in the z–y plane).

The holder is the same described in the Introduction and the voxelized mouse is embedded in the structure as is shown in Figure 3.2.

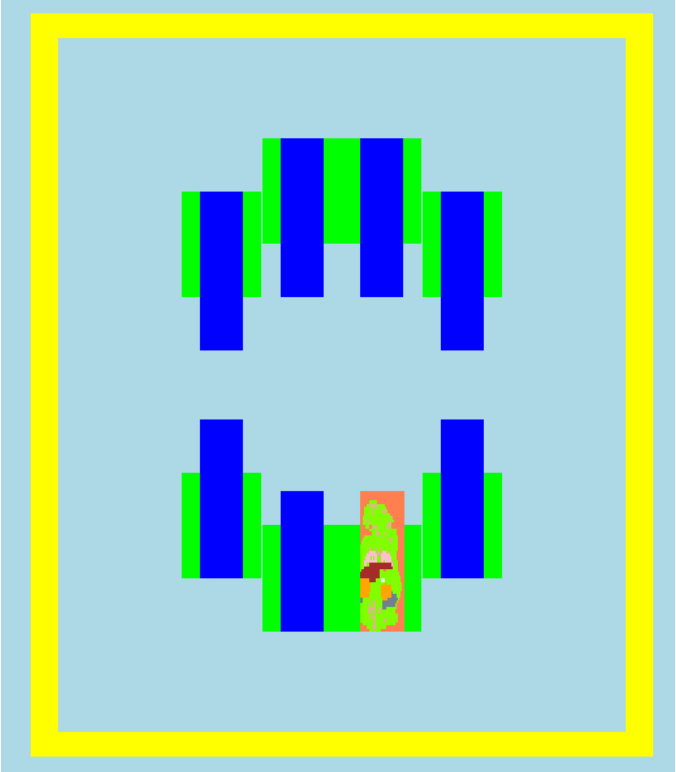

Figure 3.2: View of the mice holder with the voxelized model inserted in one of its positions.

3.3 Two case studies: Glioblastoma Multiforme and Head and Neck tumor

Two case studies have been considered, as represented in Figure 3.5. The tumor was added as a small sphere of the same tissue as the organ hosting it: in the case of the Glioblastoma the sphere has a radius of 2 mm, instead in the Head and Neck tumor the sphere has a radius equal to 1 mm. The first (Figure 3.3) is an internal tumor located within the brain, representative of a an animal model bearing a Glioblastoma. The second case (Figure 3.4) is a superficial subcutaneous tumor, representative of an animal model with a head and neck tumor. These two cases are two typical situations where the animal models may carry a tumor which develops into the organ as in human patients, or may carry a subcutaneous tumor which is artificially grown superficially. The advantage of the first model is that is more realistic, however, the follow up is more complex, requiring either the sacrifice of the animals after a certain time post-irradiation, losing the temporal evolution, or the availability of imaging systems for animals (such as micro CT scans or micro MRI). On the other hand, a subcutaneous tumor is externally visible and measurable.

As the idea is to perform a treatment planning as for the patients, an important information regards the prescription of the dose. In general, the Monte Carlo code transports neutrons and calculates the 4 components of dose rate over a mesh superimposed to the model. The prescription in BNCT is always to the most radiosensitive organ exposed to the neutron beam. When the prescription dose is reached, the irradiation must be stopped, not to overcome the tolerance dose limit. This is the way the irradiation time is decided.

A boron concentration was introduced in the description of biological tissues to account for the impact of thermal neutron absorption in the transport calculations. In particular, a concentration of 15 ppm was assumed in healthy brain tissue and in all healthy organs concerning the Glioblastoma Multiforme, whereas a higher concentration of 52.5 ppm was assigned to the tumor region, instead a concentration of 10 ppm was assumed in healthy mucosa tissue and in all healthy organs concerning the Head and Neck tumor, whereas a higher concentration of 50 ppm was assigned to the tumor region.

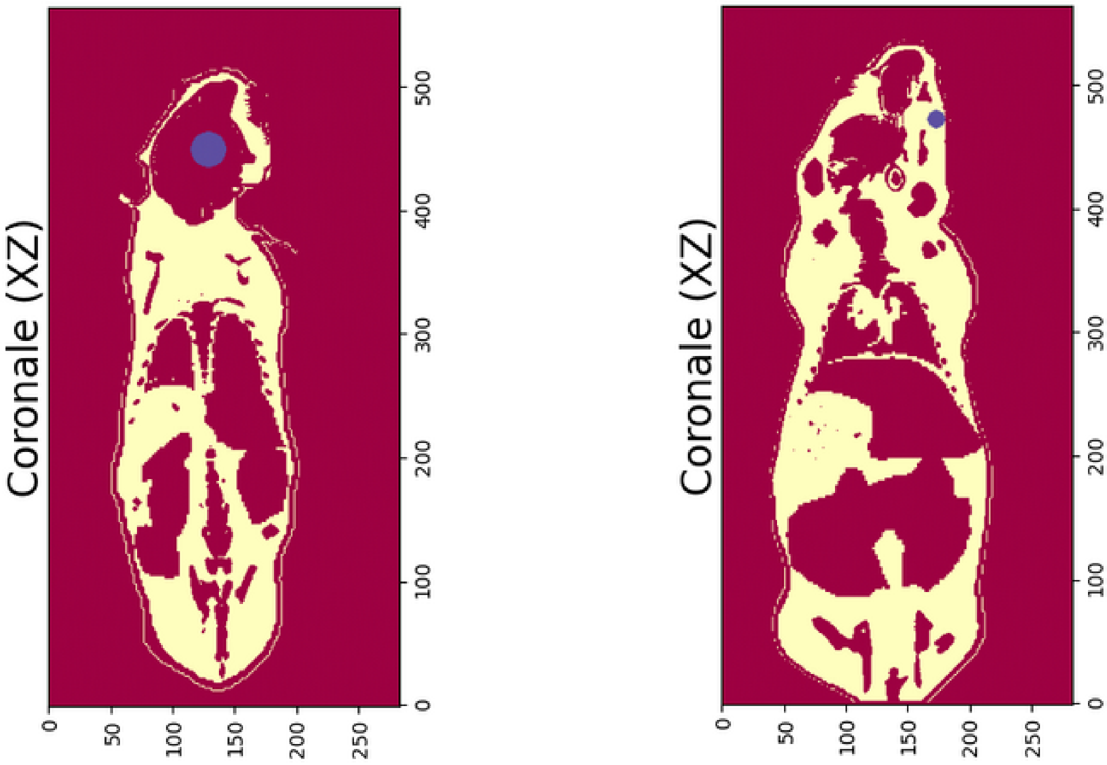

Figure 3.3: CT mouse model used in the simulations with the glioblastoma inside the brain (sectional view in the x-z plane).

Figure 3.4: CT mouse model used in the simulations with the head and neck tumor in a subcutaneous position (sectional view in the x-z plane).

Figure 3.5: IT_STARTS representation of the CT-model of the mouse with the tumor in a subcutaneous position (right) and with the tumor inside the brain (left).

At this stage, the dose rates obtained from the output file generated by the particle transport simulation are imported into a spreadsheet. This file is subsequently processed by the IT_STARTS code to compute the total absorbed dose and to provide the relevant quantities required for treatment planning. In addition to the dose rates, the spreadsheet includes the file path to the CT dataset, the boron concentration in the gross tumor volume (GTV), the definition of regions of interest (ROIs) and organs at risk (OARs), as well as the prescribed dose constraints used to determine the irradiation time. In this work, the mouse model was defined by segmenting a total of fifteen anatomical structures. These include the tumor, brain, bones, air cavities, bladder, right eye, left eye, heart, intestines, kidneys, liver, lungs, olfactory bulbs, body skin, head skin, spinal column and spleen. Figure 3.12 illustrates examples of few masks used for dose computation within the relevant regions of interest (ROIs).

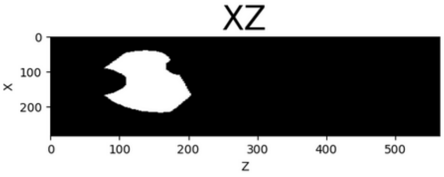

Figure 3.6: Intestine mask.

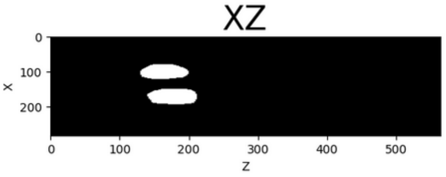

Figure 3.7: Kidneys mask.

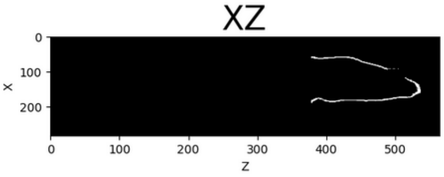

Figure 3.8: Head skin mask.

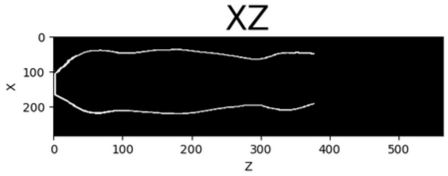

Figure 3.9: Body skin mask.

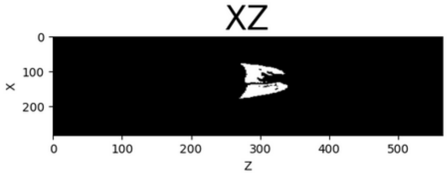

Figure 3.10: Lungs mask.

Figure 3.11: Liver mask.

Figure 3.12: Examples of masks used for treatment planning of the mouse with IT_STARTS.

For the calculation of photon-equivalent dose, IT_STARTS allows the implementation of radiobiological parameters for both the RBE-weighted dose model and the photon isoeffective dose model. The absorbed dose in the OAR is computed using the RBE-weighted formalism, adopting typically the radiobiological parameters reported by Coderre [51], which are commonly used in clinical practice ($CBE = 1.35, RBE_{\mathrm{th}} = RBE_{\mathrm{f}} = 3.2$ and $RBE_{\gamma} = 1$ for the brain and $CBE = 3.8$, $RBE_{\mathrm{th}} = RBE_{\mathrm{f}} = 3.2$ and $RBE_{\gamma} = 1$ for the GBM, instead in the second case $CBE = 2.5$, $RBE_{\mathrm{th}} = RBE_{\mathrm{f}} = 3.2$ and $RBE_{\gamma} = 1$ for the mucosa and $CBE = 3.8$, $RBE_{\mathrm{th}} = RBE_{\mathrm{f}} = 3.2$ and $RBE_{\gamma} = 1$ for the Head and Neck tumor [52]). However, other RBE factors can be implemented in IT_STARTS, provided the availability of proper radiobiological experiments, see for example [53]. Although the GTV dosimetry is evaluated using the photon isoeffective dose model, its application to the healthy tissues taken in exam in this work is not yet fully established. Nevertheless, the use of a fixed-RBE approach for healthy tissues is justified. First, the dose-limiting criteria currently adopted in clinical BNCT are based on RBE/CBE-weighted quantities. Furthermore, several studies have shown that at low dose levels, which are typical of healthy tissues, the difference between the RBE-weighted dose and the photon isoeffective dose is not significant [31].

Regarding the dosimetric approach, charged particle equilibrium (CPE) dosimetry is employed here through the use of KERMA factors. This approximation is considered valid in the present context since, as discussed in Chapter 2, the tumor is located in an internal region of the body, where the conditions for CPE are satisfied or at least the discrepancy is less significant.

3.3.1 Results for the Glioblastoma Multiforme

In the case of mice affected by Glioblastoma Multiforme, two prescription approaches are generally considered. One is based on the average dose delivered to the organ at risk (OAR), D_{mean}, while the other relies on a maximum dose constraint, D_{max}. In this work, an average dose limit of $D_{\text{mean}} = 2.5$ Gy (RBE) and a maximum dose of $D_{\text{max}} = 13$ Gy (RBE) to the brain have been assumed [54]. These two criteria correspond, respectively, to a constraint on the dose absorbed by 50% of the brain volume and to the maximum dose delivered to the most exposed region. During the treatment planning phase, both limits are evaluated and the irradiation conditions are determined by the most restrictive one, i.e., the constraint that is reached first. This ensures that both local overexposure and excessive average dose to the brain are adequately controlled. For this case, the irradiation time obtained using the criterion described is 50.21 minutes for the D_{mean} limit and 84.27 minutes for the D_{max} limit. As said above, to protect as much as possible the normal brain the software selects the lower time: 50.21 minutes.

For the GTV in the Glioblastoma Multiforme case, the photon isoeffective dose model is employed. However, for comparison purposes, the RBE-weighted dose is also reported using experimentally derived radiobiological data. These data were obtained from in vitro studies performed in Pavia on the human immortalized GBM cell line U87. The corresponding radiobiological parameters were derived from irradiation experiments conducted at the TRIGA Mark II reactor of the University of Pavia [53]. In these experiments, cell cultures treated with boronophenylalanine (BPA) were irradiated with a thermal neutron beam characterized by low gamma and fast neutron contamination, using the thermal column of the reactor. Additional samples were irradiated without boron (beam-only configuration), while reference irradiation experiments were performed using a ^{60}Co photon source available at the facility. Dose-escalation protocols were applied in all cases in order to derive cell survival curves, following the methodology described in [55]. The survival curves are presented in Figure 3.13. These curves describe the in vitro dose-response relationship for GBM cells under BNCT irradiation conditions, enabling the conversion of the delivered BNCT dose into photon-equivalent dose through the use of appropriate radiobiological parameters, both using the traditional fixed-RBE model and the photon isoeffective one.

It is worth noting that the radiobiological parameters commonly adopted in clinical practice are primarily based on the experiments performed by Coderre, which were conducted using a Gliosarcoma experimental model. The cited thesis and paper by B. Marcaccio demonstrated however the importance of using the correct biological model to infer the most robust parameters for the

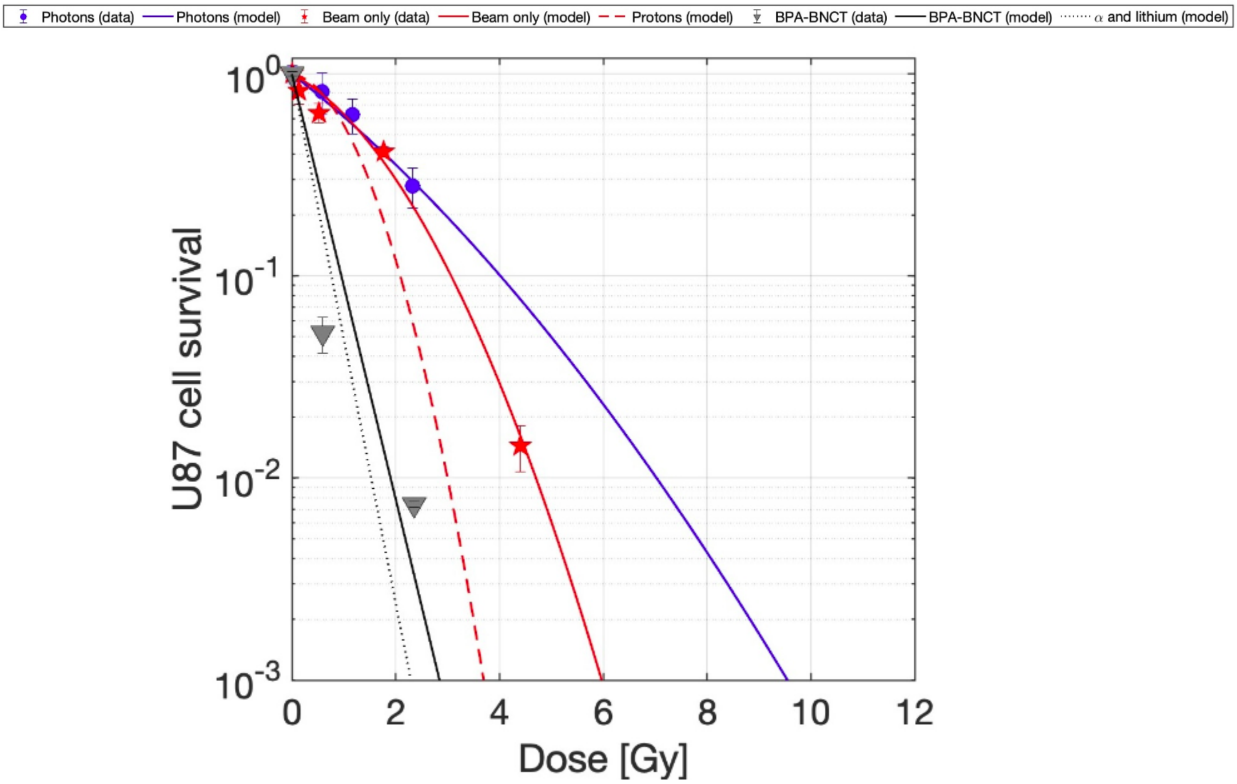

Figure 3.13: Survival curves of U-87 cells vs. absorbed dose. Blue: reference radiation ^{60}Co (dots: data, line: fit). Red: beam-only irradiation (stars: data, solid line: fit; dashed line: isolated proton contribution). Black: BPA-BNCT (triangles: data, solid line: fit; dotted line: boron-only contribution). Taken from [56]

translation of the dose in photon-equivalent units. The compound biological effectiveness (CBE) factor is determined by comparing the photon dose, represented by the blue curve, with the dose due to the boron capture reaction, depicted by the black dotted curve, for the same biological endpoint. A similar procedure is adopted for the evaluation of the relative biological effectiveness for thermal and fast neutrons (RBE_{th} and RBE_{f}). Since proton emission occurs in both reaction channels, their biological effectiveness can be assumed to be equivalent. As a consequence, a single value of RBE_n is considered, referring to the survival curve component associated exclusively with proton and ^{14}C ion contributions, represented by the dotted line.

To apply Equation 1.3 and to select a survival fraction of 1% as the biological endpoint, the compound biological effectiveness was evaluated as $\mathrm{CBE} = 6.03 \pm 0.03$, while the neutron relative biological effectiveness was determined to be $RBE_n = 4.49 \pm 0.08$. By definition, the value of $RBE_\gamma = 1$.

With regard to the photon isoeffective dose model, the characteristic repair time constants for the U87 cell line, together with the relative fractions of cells undergoing fast and slow repair kinetics for both photon and high-LET radiation components, were used as fitting parameters. The resulting values are reported below:

- t_{0f} = 91.42 min, characteristic repair time considering the fast kinetics;
- t_{0s} = 1238 min, characteristic repair time considering the slow kinetics;
- $p_{\gamma f}$ = 0.77, proportion of sublesions repaired by the fast kinetics for low-LET radiation;
- $p_{\gamma s}$ = 0.23, proportion of sublesions repaired by the slow kinetics for low-LET radiation;
- p_{BNCTf} = 0.2, proportion of sublesions repaired by the fast kinetics for high-LET radiation;
- p_{BNCTs} = 0.8, proportion of sublesions repaired by the slow kinetics for high-LET radiation.

These parameters allow the calculation of the Lea-Catcheside time dependent factor $G(\theta)$, mentioned in the Introduction, by applying the Equations 1.6 and 1.7.

The radiobiological parameters α and β, required for the photon isoeffective dose calculation (see Equation 1.10), were determined under the following assumptions:

- for photons, $\alpha_4 = \alpha_R$ and $\beta_4 = \beta_R$, due to the similarity between the energy spectrum of the reference photons (^{60}Co, approximately 1 MeV) and that of the gamma component of the neutron beam (typically around 2 MeV);
- for neutrons, $\alpha_2 = \alpha_3 = \alpha_n$ and $\beta_2 = \beta_3 = \beta_n$, where indices 2 and 3 refer to thermal and fast neutron dose contributions, respectively. This assumption is justified by the comparable energy of recoil protons generated in fast neutron interactions and those produced in the ^{14}N(n,p)^{14}C reaction induced by thermal neutrons, leading to similar biological effectiveness.

These assumptions reduce the number of independent parameters required by the model. By fitting the experimental data shown in Figure 3.13, the set of radiobiological parameters reported in Table 3.1 was obtained for the U87 cell line.

	α (Gy^{-1})	β (Gy^{-2})
Boron	2.4 ± 0.5	0
Neutrons	0.6 ± 0.6	0.5 ± 0.9
Photons	0.17 ± 0.08	0.021 ± 0.009

Table 3.1: Parameter values of the survival curves obtained by fitting the experimental data in Figure 3.13.

Finally, IT_STARTS computes the voxel-wise photon isoeffective dose distribution within the mouse using the experimentally derived parameters and generates the corresponding dose-volume histograms (DVHs), useful tools to describe the dose distribution delivered within the mouse volume of interest. Figure 3.14 presents the DVHs for both the OAR and the GTV, comparing the results obtained with the fixed-RBE and photon isoeffective dose models.

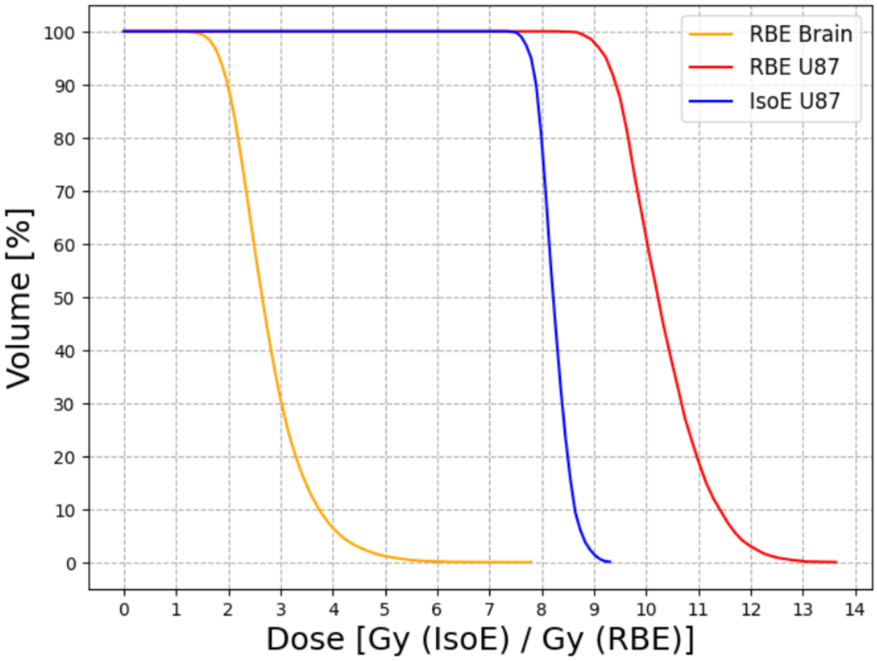

Figure 3.14: DVHs of the brain (orange line) and the GTV calculated by applying both RBE-weighted (red line) and the photon isoeffective dose (blue line) models.

The DVH of the brain, shown in Figure 3.14, reflects the dose constraint used to determine the irradiation time. A comparison between the GTV DVHs obtained using the two dosimetric models highlights significant differences, consistently with the considerations discussed before. In particular, the RBE-weighted dose model predicts substantially higher photon-equivalent doses in the tumor compared to those obtained with the photon isoeffective dose model [19].

Table 3.2 reports the minimum, mean and maximum dose values for the GTV. Among these metrics, the minimum dose plays a crucial role, as the tumor control probability is highly sensitive to under-dosed regions. An effective treatment should therefore ensure adequate dose coverage throughout the entire tumor volume. Conversely, the maximum dose within the tumor is generally less relevant for the clinical outcome.

	RBE-weighted Dose	Photon Isoeffective Dose
Minimum Dose (Gy)	9.0	7.7
Mean Dose (Gy)	10.2	8.2
Maximum Dose (Gy)	12.2	8.9

Table 3.2: Values of minimum, mean, and maximum dose calculated using the two photon-equivalent dose models. The minimum dose refers to the dose value received by 98% of the volume, the mean corresponds to the dose received by 50% and the maximum to 2% of the total volume of the GTV.

It is from considerations of this type that it was possible to test whether the RBE or the isoeffective model was the most appropriate to explain retrospective clinical outcomes through Tumor Control Probability (TCP) calculations [20, 19, 31]. In those works it was demonstrated that RBE dose model delivers higher dose in the tumor which is, in fact, not equivalent to photon therapy, as the clinical results cannot be explained in light of the RBE-weighted dose. On the other hand, photon isoeffective model allows to predict the number of controlled lesions that is expected according to the TCP model. Recently, the same considerations but applied to the Normal Tissue Complication Probability (NTCP) have led to the the same conclusions for the healthy mucosa in case of treatment of tumors in the head and neck district.

3.3.2 Results for the Head and Neck tumor

In the case of Head and Neck tumor, particular attention must be devoted to the mucosal tissues, as the target tumor is located within the mucosa. Moreover, being mucosa full of blood, it also abosrb higher boron concentrations compared to other normal tissues. Due to the high radiosensitivity of this tissue, a strict dose constraint must be imposed in order to prevent excessive toxicity. According to the clinical indications reported in the literature [8], the maximum tolerated physical dose to the mucosa is limited to 6 Gy. This constraint is applied at the point where the mucosal dose rate reaches its maximum value, which represents the most critical location in terms of potential damage to healthy tissue. Based on this condition, the irradiation time is determined by imposing that the total dose at this point does not exceed the prescribed limit. Therefore, the treatment duration is directly derived from the maximum mucosal dose rate, as described in Equation 3.1, ensuring compliance with the clinical dose constraint.

$$t = \frac{D_{\text{max}}}{\dot{D}_{\text{mucosa,max}}} \tag{3.1}$$

For this case, the irradiation time obtained using the criterion described is 39.46 minutes.

The radiobiological parameters α and β, required for the photon isoeffective dose calculation (see Equation 1.10), in this case, were adopted from the study by Gonzalez et al. [31]. Notably, the parameters for the photon isoeffective dose are not derived from in vitro survival studies, but from in vivo irradiation of hamsters bearing head and neck tumors. This study confers robustness to the photon-equivalent dose values calculated, as they are translated using directly the TCP of real tumors. The values used in this work, reported in the Table 3.3, are therefore derived from their analysis.

	α (Gy^{-1})	β (Gy^{-2})
Boron	0.331	0.0000124
Neutrons	0.342	0.0000122
Photons	0.02957	0.02957

Table 3.3: Radiobiological parameters taken from [31].

In the case of a tumor located within the mucosal region, the interpretation of dose-volume histograms (DVHs) for the mucosa requires particular caution. In the present work, the mucosa was not explicitly segmented as a well-defined anatomical structure, but rather identified as the residual volume located within the head of the mouse including all structures not assigned to the predefined masks, as shown in Figure 3.15. As a consequence, the resulting mucosal volume does not correspond to the actual physical thickness and spatial extent of the biological mucosa, which is intrinsically a very thin layer.

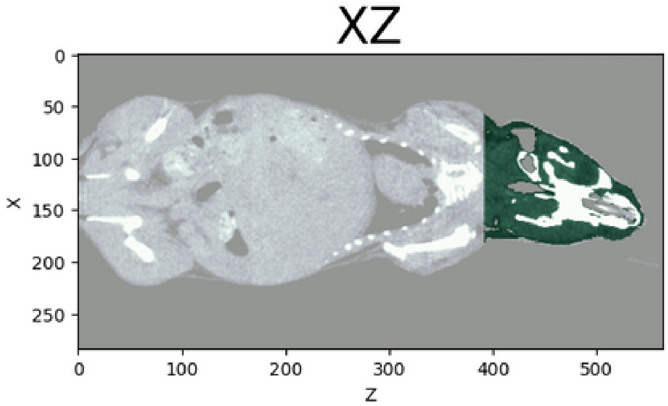

Figure 3.15: The mucosa mask, defined as the green area, identified as the residual volume of the head including all structures not assigned to the predefined masks located in the head.

This approximation leads to a conservative representation of the organ at risk, however it also limits the physical significance of the corresponding DVH. In particular, the selected voxels contributing to the highest dose regions within the so-called mucosa may in reality belong to different tissues, such as muscle, due to the lack of precise anatomical discrimination. Therefore, the DVH associated with this structure cannot be considered fully representative of the true dose distribution in the mucosal tissue.

Nevertheless, a meaningful dosimetric evaluation can still be performed by considering both the mucosa and the brain. While the mucosal DVH provides a conservative upper bound on the dose delivered to superficial tissues, the brain remains a clearly defined organ at risk and may receive a non-negligible dose contribution. For this reason, it is essential to verify that the dose delivered to the brain does not exceed the prescribed tolerance limits discussed above. In such conditions, the brain effectively becomes the limiting organ for the treatment and its DVH represents a reliable and clinically relevant indicator for treatment planning.

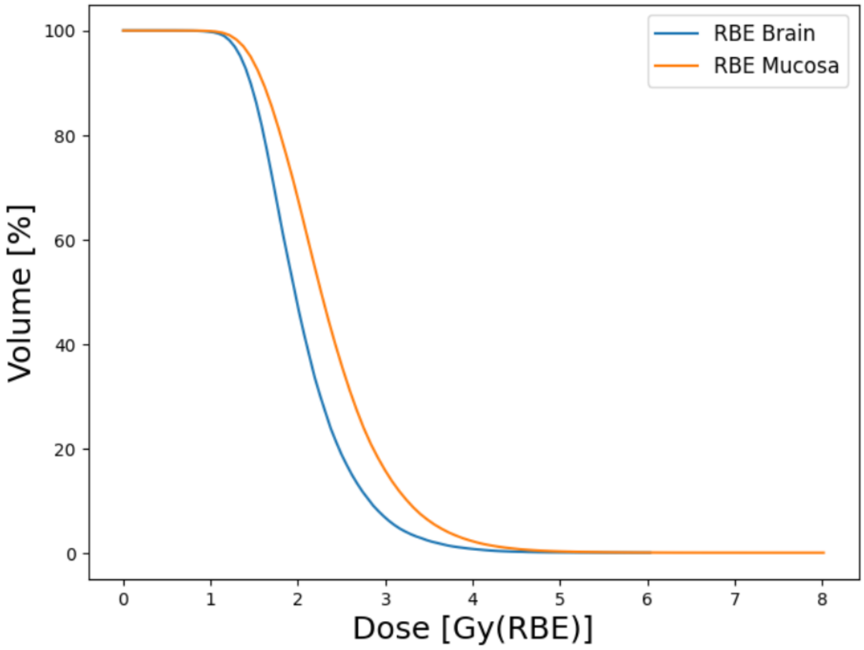

Figure 3.16: DVHs of the brain (blue line) and the mucosa calculated by applying RBE-weighted model.

As shown in Figure 3.16, the results highlight that applying dose-limitation strategies analogous to those used in clinical settings is not appropriate in the murine model. In the experimental configuration, the entire head of the mouse is uniformly irradiated, leading to a substantially different dose distribution compared to the patient scenario. In clinical practice, the neutron beam can be accurately positioned and shaped to target the tumor region as closely as possible, thereby sparing surrounding healthy tissues. This fundamental difference implies that organ-at-risk considerations derived from patient treatments cannot be directly translated to the murine case, where the irradiation geometry inherently lacks the same level of spatial selectivity.

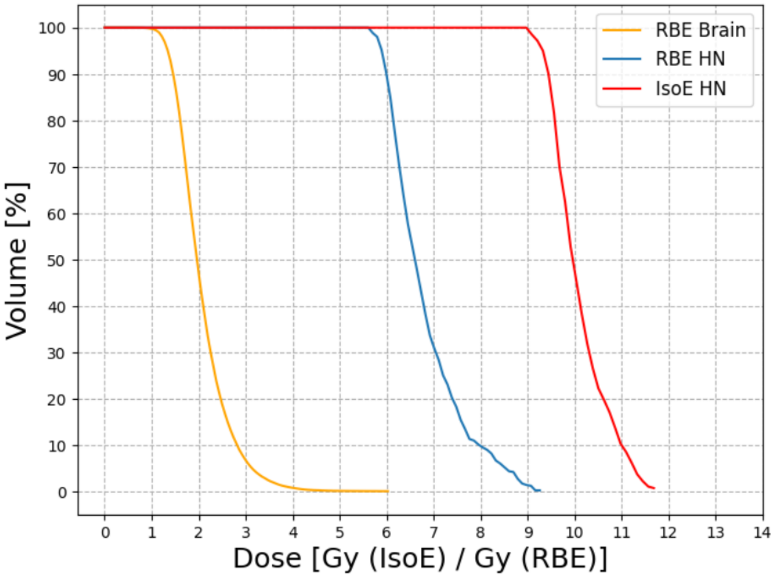

Figure 3.17: DVHs of the brain (orange line) and the GTV calculated by applying both RBE-weighted (blue line) and the photon isoeffective dose (red line) models.

The DVH comparison, shown in Figure 3.17, highlights that the separation between the tumor and healthy brain curves could, in principle, be significantly improved. In fact, a detailed analysis of the dose components responsible for limiting the irradiation reveals that the dominant contribution arises from photons. This indicates that the total dose is largely driven by the photon that are a non-selective component, which affects both tumor and healthy tissues in a similar manner. As a consequence, the intrinsic selectivity of the boron capture reaction is not fully exploited, since the photon dose contributes substantially also within the tumor volume, thereby reducing the achievable therapeutic gain. Clearly the holder introduces a non-negligible photon background that limits the effectiveness of the treatment planning. The photon production within the holder appears to compromise the dose differential between tumor and normal tissue, preventing an optimal enhancement of the biologically effective dose in the target. Therefore, these results point to the need for a careful evaluation and possible optimization of the holder design, with the aim of minimizing parasitic photon generation and improving the overall selectivity of the BNCT irradiation. This also explains why the photon isoeffective dose is larger than the RBE-weighted dose: we are in a dose range where this can happen, as in normal tissues of patients [19].

Retrospectively, it makes sense to verify whether mucosa could represent a limiting constraint also in the case of a brain tumor. Referring to the previously computed dose rates, applying the maximum physical dose rate obtained for the mucosa with the irradiation time obtained for the Glioblastoma Multiforme case (50.21 minutes), the mucosa would receive a total physical dose of 8.90 Gy, exceeding the prescribed tolerance limit of 6 Gy. This indicates that, if mucosal toxicity were strictly enforced as a limiting criterion, the irradiation time should be reduced to 39.46 minutes in order to preserve this tissue.

It is important to note, however, that the definition of mucosa adopted in this work is not anatomically precise. As described above, the mucosal region was approximated as the residual volume obtained by subtracting the set of predefined anatomical masks from the whole body. Consequently, this region may include tissues that do not physically correspond to mucosa.

For this reason, a further investigation was performed to identify where, in the so-defined mucosa, it is receive the maximum dose. As shown in Figure 3.18, the corresponding point is likely located in a region that, under a more refined anatomical segmentation, would not be classified as mucosal tissue. Therefore, the associated dose value may represent an overestimation of the actual dose delivered to the mucosa.

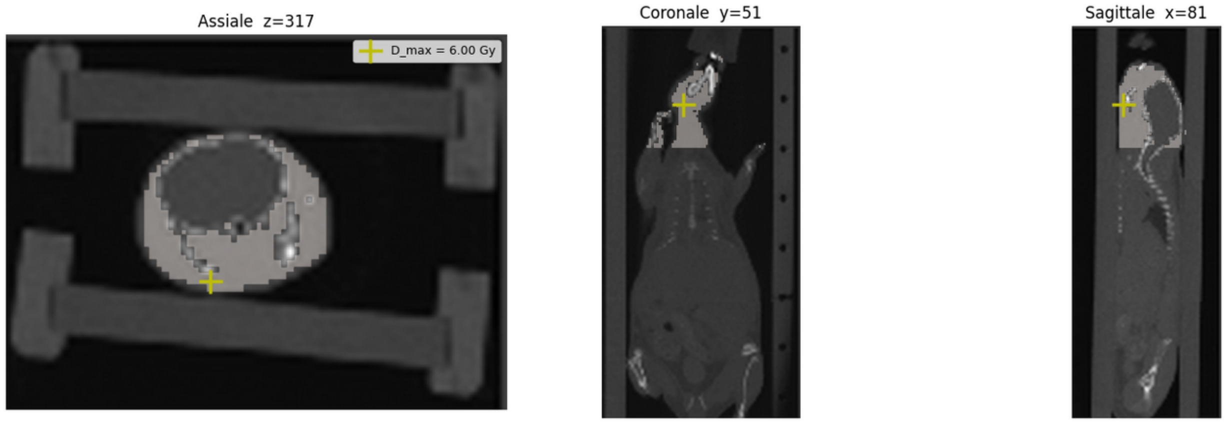

Figure 3.18: CT representation of the mouse with the location of the maximum dose highlighted by a yellow cross.

Thanks to these considerations, the mucosal constraint derived in this manner should be interpreted as conservative. A more accurate anatomical definition of the mucosa would likely lead to a less restrictive condition, potentially allowing irradiation times closer to those determined based on the brain dose limits.

The same calculations will be repeated for the neutron beam of the Finnish facility and the results will be inter-compared with the aim of understanding the differences in animal radiobiological results and dosimetry according to different beamlines.

Chapter 4

Conclusion and Future Works

The work performed in this thesis concerned the preparation of in vivo radiobiological studies for accelerator-based BNCT. First, a dedicated holder was designed and tested in Finland for the hosting of alive animal, compliant with the dosimetric requirements and the animal well-being regulation. This holder needs to thermalize the beam in order to maximize the probability of boron capture in the tumor. Being the animals very small, the clinical epithermal beam would not meet this criterion. Then, the treatment planning system IT_STARTS developed in Pavia was applied to perform the simulation of animal irradiation. The idea was to test if a software built for patients treatment planning is a suitable tool also to make a more refined simulation of in vivo experiments, allowing the analysis of the dosimetry in the body of the animals with the same methods as for human patients. This would allow a more profound understanding of the biological outcome as a function of the absorbed dose and with information regarding the dose distribution in all the organs.

The IT_STARTS computational tool has proven to be a powerful and versatile framework for BNCT treatment planning in preclinical settings. Unlike conventional clinical treatment planning systems, which are not designed to handle small animal models, IT_STARTS enables a complete workflow starting from the CT imaging of the mouse model up to the generation of dose-volume histograms (DVHs). This capability represents a significant advantage, as it allows for a detailed and patient-specific dosimetric and radiobiological analysis in animal experiments.

The integration of imaging data, dose calculations and radiobiological modeling provides a more realistic and quantitative description of the irradiation scenario. In particular, the possibility of incorporating biologically relevant parameters contributes to bridging the gap between purely physical dose estimation and the actual biological response, thus offering a more reliable basis for interpreting experimental outcomes. As a result, this approach enhances the ability to optimize irradiation conditions and to better understand the dose-effect relationship in view of translational applications. On one hand, biological outcome as a function of the absorbed dose will be the input to generate photon isoeffective dose calculations with new data and with the relevant neutron beam. On the other hand, the possibility to generate a detailed dose-response evaluation will enable the verification of the true photon-isoeffectiveness of BNCT prescribed dose.

The work presented here should be regarded as a preliminary step toward forthcoming in vivo irradiation experiments. In particular, the developed methodology is intended to support experiments involving animal models placed within irradiation holder, optimized thanks to this work, at the Helsinki Hospital. The same holder could be also used in the ANTHEM BNCT facility currently under development in Caserta. The capability to produce an animal treatment planning will be beneficial for these two facilities and for others that might adopt this computational tool.

Due to circumstances beyond the control of this work, it was not possible to include the results obtained with the Finnish neutron source within the present study. Nevertheless, such data are expected to become available in the near future and will be analyzed following the same methodological framework developed in this thesis. This will enable a consistent comparison and provide further insight into how the irradiation setup, and in particular the animal holder, can be optimized and adapted to the specific characteristics of the neutron source.

Future work will focus on refining the anatomical modeling, improving the definition of radiobiological parameters and validating the computational predictions against experimental data. In this context, the results indicate that, although a certain degree of selectivity can be achieved in BNCT, the current setup remains not optimal. In particular, the photon dose component generated within the irradiation holder introduces a significant non-selective contribution, limiting the achievable dose differential between tumor and healthy tissues. This suggests that targeted improvements in the holder design, such as the inclusion of internal high-Z shielding layers (e.g. lead) to attenuate photons, could enhance treatment effectiveness by reducing the non-selective dose component.

More broadly, the comparison between different irradiation facilities will be essential to ensure the flexibility and robustness of the proposed approach, while the detailed treatment planning framework adopted in this work provides valuable feedback on the adequacy of the experimental setup. This combined strategy will guide targeted modifications of the holder design and ultimately strengthen the connection between preclinical investigations and clinical applications.

Bibliography

[1] *Advances in Boron Neutron Capture Therapy*. TECDOC Series. Vienna: INTERNATIONAL ATOMIC ENERGY AGENCY, 2023.

[2] AG Vladimirov et al. “Synthesis of composite Si-B nanoparticles by the laser-induced pyrolysis method”. In: *Laser Physics Letters* 11.12 (2014), p. 126002.

[3] Yutaka Mishima Masamitsu Ichihashi Takafumi Nakanishi. “Specific killing effect of 10b1-paraboronophenylalanine in thermal neutron capture therapy of malignant melanoma: in vitro radiobiological evaluation.” In: *Journal of Investigative Dermatology* (1982), pp. 215–218.

[4] Fukuda H et al. “Boron neutron capture therapy of malignant melanoma using 10B - paraboronophenylalanine with special reference to evaluation of radiation dose and damage to the normal skin”. In: *Radiation Research* (1994), pp. 435–442.

[5] M. Sato et al. “Safety of Boron Neutron Capture Therapy with Borofalan(10B) and Its Efficacy on Recurrent Head and Neck Cancer: Real-World Outcomes from Nationwide Post-Marketing Surveillance”. In: *Cancers* 16 (5 2024), p. 869.

[6] Yi-Wei Chen et al. “Salvage Boron Neutron Capture Therapy for Malignant Brain Tumor Patients in Compliance with Emergency and Compassionate Use: Evaluation of 34 Cases in Taiwan”. In: *Biology* 10.4 (2021).

[7] Andres Juan Kreiner et al. “Present status of accelerator-based BNCT”. In: *Reports of Practical Oncology & Radiotherapy* 21.2 (2016), pp. 95–101.

[8] Leena Kankaanranta et al. “Boron neutron capture therapy in the treatment of locally recurred head-and-neck cancer: final analysis of a phase I/II trial”. In: *International Journal of Radiation Oncology* Biology* Physics* 82.1 (2012), e67–e75.

[9] Liisa Porra et al. “From Nuclear Reactor-Based to Proton Accelerator-Based Therapy: The Finnish Boron Neutron Capture Therapy Experience”. In: *CANCER BIOTHERAPY AND RADIOPHARMACEUTICALS* 38.3 (2023), pp. 184–191.

[10] A Pisent et al. “ANTHEM project, construction of a RFQ driven BNCT neutron source”. In: *Proc. LINAC2024, Chicago, IL, USA* (2024).

[11] E Fagotti A Pisent and P Colautti. “MUNES a compact neutron source for BNCT and radioactive wastes characterization”. In: *Proc. Linear Accelerator Conf. LINAC.* (2014), pp. 261–263.

[12] Ian Postuma et al. “A novel approach to design and evaluate BNCT neutron beams combining physical, radiobiological, and dosimetric figures of merit”. In: *Biology* 10.3 (2021), p. 174.

[13] Giovanni Garini et al. "Evaluation of patient activation and dosimetry after Boron Neutron Capture Therapy". In: *arXiv preprint arXiv:2501.13053* (2025).

[14] AA.VV. "ICRU Report 44: Tissue Substitutes in Radiation Dosimetry and Measurement". In: *Journal of the ICRU* (1989).

[15] H. Kumada and K. Taka. "Treatment planning system and patient positioning for boron neutron capture therapy". In: *Therapeutic Radiology and Oncology* (2018).

[16] B. Marcaccio et al. "Unraveling the role of boron microdistribution in BNCT dosimetry of Glioblastoma Multiforme: combined theoretical and experimental insights". In: *accepted by Physics in Medicine and Biology* (2026).

[17] J.A. Coderre et al. "Derivations of relative biological effectiveness for the high-let radiations produced during boron neutron capture irradiations of the 9L rat gliosarcoma in vitro and in vivo". In: *International Journal of Radiation Oncology Biology Physics* (1993), pp. 1121–1129.

[18] Sara J. González and Gustavo A. Santa Cruz. "The photon-isoeffective dose in boron neutron capture therapy". In: *Radiation research* (2012).

[19] Sara J. González and Gustavo A. Santa Cruz. "The photon-isoeffective dose in boron neutron capture therapy". In: *Radiation research* (2012).

[20] Giuliano Franco Perotti Bernardini et al. "Comparison of photon isoeffective dose models based on in vitro and in vivo radiobiological experiments for head and neck cancer treated with bnct". In: *Radiation Research* 198.2 (2022), pp. 134–144.

[21] Frank Herbert Attix. *Introduction to radiological physics and radiation dosimetry*. John Wiley & Sons, 2008.

[22] WILLIAM Parker and HORACIO Patrocinio. "Clinical treatment planning in external photon beam radiotherapy". In: *Radiation oncology physics: A handbook for teachers and students. Vienna: IAEA* 219 (2005).

[23] D. Jones. "ICRU Report 50-Prescribing, Recording, and Reporting Photon Beam Therapy". In: *Journal of the ICRU* 21 (1994).

[24] A. Wambersie. "ICRU Report 62, Prescribing, Recording and Reporting Photon Beam Therapy (Supplement to ICRU 50)". In: *Journal of the ICRU* 32 (1999).

[25] P. Mayles, A. Nahum, and J.C. Rosenwald. *Handbook of radiotherapy physics: theory and practice*. CRC Press, 2007.

[26] Wolfgang Sauerwein et al. *Neutron capture therapy: principles and applications*. Springer, 2012.

[27] C. J. Werner (editor). "MCNP Users Manual - Code Version 6.2". In: *Los Alamos National Laboratory, Los Alamos, NM, report LA-UR-17-29981* (2022).

[28] Tatsuhiko Sato et al. "Features of Particle and Heavy Ion Transport code System (PHITS) version 3.02". In: *Journal of Nuclear Science and Technology* 55 (Jan. 2018), pp. 1–7. DOI: `10.1080/00223131.2017.1419890`.

[29] R.O. Farias and S.J. González. "MultiCell model as an optimized strategy for BNCT treatment planning". In: (2012), pp. 10–14.

[30] Rubén O Farías et al. "Exploring boron neutron capture therapy for non-small cell lung cancer". In: *Physica Medica* 30.8 (2014), pp. 888–897.

[31] SJ González et al. "Photon iso-effective dose for cancer treatment with mixed field radiation based on dose-response assessment from human and an animal model: clinical application to boron neutron capture therapy for head and neck cancer". In: *Physics in Medicine & Biology* 62.20 (2017), p. 7938.

[32] Ian Postuma et al. "Using the photon isoeffective dose formalism to compare and combine BNCT and CIRT in a head and neck tumour". In: *Scientific Reports* 14.1 (2024), p. 418.

[33] Ana Mailén Dattoli Viegas et al. "Predicting radiotoxic effects after BNCT for brain cancer using a novel dose calculation model". In: *Physica Medica* 128 (2024), p. 104840.

[34] Shumin Shen et al. "A clinician's perspective on boron neutron capture therapy: promising advances, ongoing trials, and future outlook". In: *International journal of radiation biology* 100.8 (2024), pp. 1126–1142.

[35] Peeter Karihtala. "The current status and future perspectives of clinical boron neutron capture therapy trials". In: *Health and Technology* 14.5 (2024), pp. 1001–1005.

[36] Manjeet Chadha et al. "Boron neutron-capture therapy (BNCT) for glioblastoma multiforme (GBM) using the epithermal neutron beam at the Brookhaven National Laboratory". In: *International Journal of Radiation Oncology* Biology* Physics* 40.4 (1998), pp. 829–834.

[37] Toshihiko Kuroiwa[a], Minoru Suzukib, and Koji Onob. "Boron neutron capture therapy of malignant gliomas". In: *Intracranial Gliomas Part III-Innovative Treatment Modalities* 32 (2018), pp. 48–56.

[38] Shinji Kawabata et al. "Boron neutron capture therapy for newly diagnosed glioblastoma". In: *Journal of radiation research* 50.1 (2009), pp. 51–60.

[39] T Kageji et al. "Clinical results of boron neutron capture therapy (BNCT) for glioblastoma". In: *Applied Radiation and Isotopes* 69.12 (2011), pp. 1823–1825.

[40] Hiroshi Hatanaka and Yoshinobu Nakagawa. "Clinical results of long-surviving brain tumor patients who underwent boron neutron capture therapy". In: *International Journal of Radiation Oncology* Biology* Physics* 28.5 (1994), pp. 1061–1066.

[41] Tetsuya Yamamoto, Kei Nakai, and Akira Matsumura. "Boron neutron capture therapy for glioblastoma". In: *Cancer letters* 262.2 (2008), pp. 143–152.

[42] T Yamamoto et al. "The status of Tsukuba BNCT trial: BPA-based boron neutron capture therapy combined with X-ray irradiation". In: *Applied Radiation and Isotopes* 69.12 (2011), pp. 1817–1818.

[43] Shinji Kawabata et al. "Accelerator-based BNCT for patients with recurrent glioblastoma: a multicenter phase II study". In: *Neuro-oncology advances* 3.1 (2021), vdab067.

[44] Teruhito Aihara and Norimasa Morita. "BNCT for advanced or recurrent head and neck cancer". In: *Neutron Capture Therapy: Principles and Applications*. Springer, 2012, pp. 417–424.

[45] Satoshi Takeno et al. "Preliminary outcomes of boron neutron capture therapy for head and neck cancers as a treatment covered by public health insurance system in Japan: real-world experiences over a 2-year period". In: *Cancer medicine* 13.11 (2024), e7250.

[46] Xing Sun et al. "Efficacy and safety of boron neutron capture therapy for locally recurrent head and neck cancer". In: *Critical Reviews in Oncology/Hematology* (2025), p. 105101.

[47] Minoru Suzuki et al. "Boron neutron capture therapy outcomes for advanced or recurrent head and neck cancer". In: *Journal of radiation research* 55.1 (2014), pp. 146–153.

[48] Ling-Wei Wang et al. “Fractionated BNCT for locally recurrent head and neck cancer: Experience from a phase I/II clinical trial at Tsing Hua Open-Pool Reactor”. In: *Applied Radiation and Isotopes* 88 (2014), pp. 23–27.

[49] Erica Simeone. “Studi dosimetrici per la BNCT del Glioblastoma Multiforme con acceleratore”. Master’s thesis. University of Pavia, 2021.

[50] Cristina Pezzi. “Comparison of dose distributions in BNCT treatment of brain tumors using human or AI-segmented medical images”. 2022. University of Pavia, 2019.

[51] Jeffrey A. Coderre and Gerard M. Morris. “The Radiation Biology of Boron Neutron Capture Therapy”. In: *Radiation Research Society* 151 (1999), pp. 1–18.

[52] Hanna Koivunoro et al. “Boron neutron capture therapy for locally recurrent head and neck squamous cell carcinoma: An analysis of dose response and survival”. In: *Radiotherapy and Oncology* 137 (2019), pp. 153–158.

[53] Barbara Marcaccio et al. “Towards an adequate description of the dose-response relationship in BNCT of glioblastoma multiforme”. In: *Medical Physics* 55 (2025), pp. 2606–2617.

[54] Young-soon Bae et al. “Advances of LINAC-based boron neutron capture therapy in Korea”. In: *AAPPS Bulletin* 32.1 (2022), p. 34.

[55] Ana Mailén Dattoli Viegas et al. “Detailed dosimetry calculation for in-vitro experiments and its impact on clinical BNCT”. In: *Physica Medica* 89 (2021), pp. 282–292.

[56] Barbara Marcaccio et al. “A multiscale dosimetric approach to BNCT for Glioblastoma Multiforme: a theoretical and experimental journey from cell microdosimetry to patient treatment”. In: (2026).